Denise Prutsch, Stefan Breuer, Marlena Uitz, Patrick Bottke, Julia Langer, Sarah Lunghammer, Martin Philipp, Patrick Posch, Veronika Pregartner, Bernhard Stanje, Andreas Dunst, Dominik Wohlmuth, Harald Brandstätter, Walter Schmidt, Viktor Epp, Alan Chadwick, Ilie Hanzu* and Martin Wilkening*

Nanostructured Ceramics: Ionic Transport and Electrochemical Activity

A short journey across various families of materials

DOI 10.1515/zpch-2016-0924
Received November 4, 2016; accepted May 23, 2017

Abstract: Ceramics with nm-sized dimensions are widely used in various applications such as batteries, fuel cells or sensors. Their oftentimes superior electrochemical properties as well as their capabilities to easily conduct ions are, however, not completely understood. Depending on the method chosen to prepare the materials, nanostructured ceramics may be equipped with a large area fraction of interfacial regions that exhibit structural disorder. Elucidating the relationship between microscopic disorder and ion dynamics as well as electrochemical performance is necessary to develop new functionalized materials. Here, we highlight some of the very recent studies on ion transport and electrochemical properties of nanostructured ceramics. Emphasis is put on TiO_2 in the form of nanorods, nanotubes or being present as mesoporous material. Further examples deal with

***Corresponding authors: Ilie Hanzu and Martin Wilkening,** Institute for Chemistry and Technology of Materials, and Christian Doppler Laboratory for Lithium Batteries, Graz University of Technology (NAWI Graz), Stremayrgasse 9, A-8010 Graz, Austria; and Leibniz University of Hannover, Institute of Physical Chemistry and Electrochemistry, Callinstraße 3-3a, D-30167 Hannover, Germany, e-mail: hanzu@tugraz.at (I. Hanzu); wilkening@tugraz.at (M. Wilkening)
Denise Prutsch, Stefan Breuer, Marlena Uitz, Patrick Bottke, Julia Langer, Sarah Lunghammer, Martin Philipp, Patrick Posch, Veronika Pregartner, Bernhard Stanje, Andreas Dunst, Dominik Wohlmuth, Harald Brandstätter, Walter Schmidt and Viktor Epp: Institute for Chemistry and Technology of Materials, and Christian Doppler Laboratory for Lithium Batteries, Graz University of Technology (NAWI Graz), Stremayrgasse 9, A-8010 Graz, Austria; and Leibniz University of Hannover, Institute of Physical Chemistry and Electrochemistry, Callinstraße 3-3a, D-30167 Hannover, Germany
Alan Chadwick: School of Physical Sciences, University of Kent, Canterbury, Kent CT2 7NH, UK

nanocrystalline peroxides such as Li_2O_2 or nanostructured oxides (Li_2TiO_3, $LiAlO_2$, $LiTaO_3$, Li_2CO_3 and $Li_2B_4O_7$). These materials served as model systems to explore the influence of ball-milling on overall ionic transport.

Keywords: amorphous materials; conductivity; glasses; lithium ion transport; nanocrystalline oxides; nanotubes; NMR; peroxides; self-diffusion; titania.

1 Introduction and motivation

The mobility of small cations or anions in ionic crystals depend on numerous factors. On the one hand, point defects and polyhedral connections play a decisive part in enabling local jump processes and bulk ion transport. On the other hand, the morphology of the whole ceramic will determine migration of the charge carriers over long, i.e. macroscopic, distances. Disorder can be introduced through many different approaches such as radiation or bombardment techniques. A far more simple approach is to mechanically treat the coarse-grained samples in high-energy mills [1]. Conveniently, high-energy ball milling is carried out at ambient temperature; it allows for the preparation of large quantities. In many cases, if only one component is treated phase pure nanocrystalline materials are obtained with large volume fractions of amorphous regions or at least disordered interfaces [2]. The introduction of point defects and dislocations is, however, also expected for the crystalline cores of the nanocrystallites [3]. So far, many examples have been reported documenting that the ionic conductivity of a poor conductor can significantly be enhanced when transforming the oxides or sulfides into a defect-rich nanocrystalline ceramics [4, 5]. One may regard the excessive generation of defects, greatly exceeding the thermodynamic level, as a possibility to form materials with metastable properties concerning both defect concentrations and non-equilibrium local structures [6–9]. In general, the interfaces in nanostructured ceramics and nano-composites may govern macroscopic properties such as the ionic and electronic conductivity [2, 10–26].

Besides such top-down approaches the direct preparation of nanocrystalline or amorphous ceramic through wet chemical methods or electrochemical techniques is also possible. As an example, the ionic conductivity of sol–gel synthesis of nanocrystalline $LiNbO_3$ is indeed enhanced compared to its single crystalline or microcrystalline form with µm-sized crystallites [4]. Considering, however, the chemically identical samples prepared by heavy ball-milling their ion conductivity is much higher. Obviously, at least in the case of poorly conducting oxides the disordered if not completely amorphous regions are greatly responsible for the

gradual transformation from a poor to a moderate or even highly conducting ion conductor [2, 5, 27–33].

Amorphous regions also immensely influence the electrochemical activity of otherwise poorly active materials. The different modifications of TiO_2 belong to such a class of materials. Only downsizing the crystallite size unlocks the full potential of anatase, rutile or TiO_2-B as anode materials [34–37]. The short diffusion lengths for both ions and electrons transform the transition metal oxide into powerful anode materials showing high rate capabilities and excellent specific charge capacities [34, 35]. This also holds for mesoporous [38, 39] and amorphous TiO_2. In the following we will report on the preparation of amorphous TiO_2 nanotubes via anodic etching [40, 41]. The nanotubes, differing in lengths according to the synthesis conditions, have been investigated with respect to loading with Li and Na ions [42]. Electrochemical investigations using cyclic voltammetry and galvanostatic cycling allowed us to reveal the underlying Na storage mechanism. Li nuclear magnetic resonance (NMR) has been used to evaluate the Li self-diffusion parameters of various electrochemically prepared, mixed-conducting Li_xTiO_2 samples [43–45]. For comparison, Li ion dynamics in mesoporous anatase was studied via spin-lock and stimulated echo NMR [43]. It turned out that Li ion diffusion is unaffected by the phase transformation from anatase to orthorhombic TiO_2 during Li uptake. This result is highly beneficial to enable stable cycling conditions in lithium-ion batteries.

The influence of structural disorder generated through ball milling on ion transport will be discussed for a range of model substances that include nanocrystalline Li_2O_2 [29], Na_2O_2 [46], the ternary oxides $LiAlO_2$ [47], Li_2TiO_3 [27], $LiTaO_3$ [5, 48], Li_2CO_3, as well as the glass former $Li_2B_4O_7$ [28]. Whereas Li ion transport in the materials mentioned above is isotropic, transition metal dichalcogenides such as SnS_2 or TiS_2 crystallize with a layered structure. Chemical lithiation enables the insertion of Li ions into the van der Waals gap between the SnS_2 sheets. The Li ions are expected to diffuse quickly along two dimensions. Preliminary NMR results on Li_xSnS_2 show how the diffusion parameters are altered when the material is exposed to mechanical treatment in ball mills. In contrast to microcrystalline Li_xSnS_2 with its fast but spatially confined 2D diffusion [49], in nanocrystalline Li_xSnS_2 the large number of Li ions in the disordered interfacial regions remarkably influence the NMR response. NMR line shapes point to a two-spin reservoir with fast and slow Li species, see also Ref. [50]. Finally, the effect of high-energy ball-milling on ion transport in $Li_2B_4O_7$ is shown. A significant difference is seen when comparing ionic conductivities of crystalline, nanocrystalline and amorphous $Li_2B_4O_7$. The strategy of introducing structural disorder and stress is useful to transform a poor ion conductor into a moderate one. For very fast ion conductors the situation is, on the other hand, expected to be different.

2 Case studies: from oxides to peroxides and back again

2.1 Electrochemical performance and Li ion transport in various forms of TiO_2

The different modifications of TiO_2 represent promising anode materials that provide hosts to reversibly store small cations such as Li and Na. If present in nanostructured form good rate capabilities and discharge capacities as high as 250 mAh/g were reported [36, 37]. Since such electrochemical properties might be linked also to ion dynamics several NMR studies took up the challenge to quantify Li self-diffusivity via, e.g. relaxometry, stimulated echo spectroscopy or even by 2D exchange spectroscopy [43–45, 51, 52]. In the following some recent studies on amorphous TiO_2 nanotubes, rutile nanorods and mesoporous TiO_2 will be presented that deal with electrochemical properties, mechanisms and ion dynamics in these spatially confined structures.

2.1.1 Amorphous TiO_2 nanotubes: synthesis, ionic diffusivity and the underlying storage mechanisms

The synthesis of anodic titania nanotubes [53–55] follows a top-down approach, self-assembled TiO_2 nanotubes are formed on titanium metal substrates by an anodic electrochemical oxidation process, called anodization. The anodization is usually done in two electrode cells at relatively high voltages, typically ranging from 10 to 200 V. To obtain the required nanotubular morphology, the anodization bath must also contain a Ti^{4+} complexing agent. The most used is F^- with which Ti^{4+} is able to form the soluble $[TiF_6]^{2-}$, see Ref. [56]. The formation of the tubes involves two opposite but balanced processes: (i) the electrochemical formation of TiO_2 and (ii) the chemical etching of the formed oxide by the complexing agent. Under high electric field conditions the anodization results in highly regular layers consisting of parallel TiO_2 nanotubes that grow from the Ti substrate.

Both aqueous-based and organic-based baths have been reported to yield highly regular nanotubular layers. While in aqueous baths the length of the nanotubes is somehow limited to 2–3 μm due to the faster fluoride etching of the electrochemically formed TiO_2, in viscous organic-based baths, e.g. ethylene glycol, it is possible to grow very long nanotubes, sometimes longer than 1 mm [57], while keeping almost the same diameter over the entire length of the nanotubes,

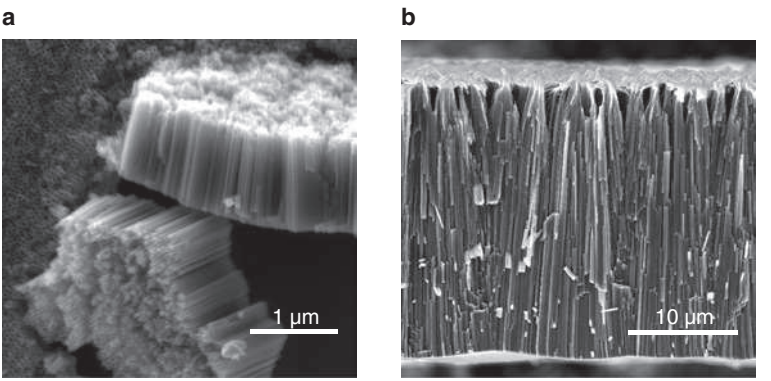

Fig. 1: Scanning electron microscopy (SEM) images illustrating the typical morphology of self-assembled TiO_2 nanotubes fabricated by electrochemical oxidation of Ti metal foil. (a) Top-view and cross-section of a TiO_2 nanotube layer obtained by anodization in an organic electrolyte bath (97.6 wt% ethylene glycol, 2 wt% water, 0.4 wt% NH_4F) at 30 V for 30 min. (b) Cross-section through a TiO_2 nanotube layer fabricated by anodization at 60 V for 1 h 30 min using the same bath composition. While the highly parallel tubular morphology is maintained when the anodization voltage is varied, the rates at which the tubes grow highly depend on the voltage applied.

typically 80–120 nm. Thus, nanotube aspect ratios of $1{:}10^4$ are easily achievable. Since the volume of the produced oxide is larger than the volume of the Ti metal from which it originated, the nanotubes are approximately 1.5 times longer than the corresponding thickness of the Ti layer consumed during anodization [58]. An illustration of some typical anodic TiO_2 nanotubes fabricated in ethylene glycol baths is presented in Figure 1.

Although the relation between the electrochemical conditions and the dimensions and geometry of the anodic titania nanotubes is a relatively complicated topic [58, 59], for a given bath, there is a direct connection between the voltage applied and the tube diameters. In principle, the higher the voltage, the larger the tube diameters are. By this method the diameters can easily be adjusted in practice between 30 and 120 nm.

One of the striking features of anodic TiO_2 is its amorphous structure [59]. In their pristine form, the nanotubes do not present any X-ray reflections in a diffraction experiment as illustrated in Figure 2. In fact, anodic titania is one of the very few known instances in which TiO_2 occurs in its amorphous form. Their unique and tunable morphology doubled by the rare amorphous structure have attracted significant attention; many scientific and technological developments based on titania nanotubes have been brought forward in the last decade [59]. One interesting development is related to the insertion in anodic TiO_2 of ionic

species such as H^+ [60], Li^+ [40] and Na^+ [42] pertaining to the broader field of energy storage and conversion. Whereas earlier NMR studies focused on Li ion diffusion in crystalline nanotubes of TiO_2, mainly TiO_2-B, that were prepared by hydrothermal routes, so far less information is available on Li^+ ion dynamics in amorphous titania nanotubes. Anodic etching allowed the preparation of relatively large quantities and, as mentioned above, according to the exact synthesis conditions both the length and the diameter of the tubes can be controlled. Li is then inserted either electrochemically in half cells with Li metal as anode material or chemically with *n*-BuLi in hexane.

For our first NMR experiments on amorphous TiO_2 rather long tubes (250 µm, see Figures 2a) were synthesized. X-ray powder diffraction confirmed the amorphous structure of the material, Figure 2b, the corresponding pattern for the pristine sample only shows reflections of the Ti metal substrate. Interestingly, the tubes remain amorphous up to 200 °C, at higher temperatures they can be converted into anatase.

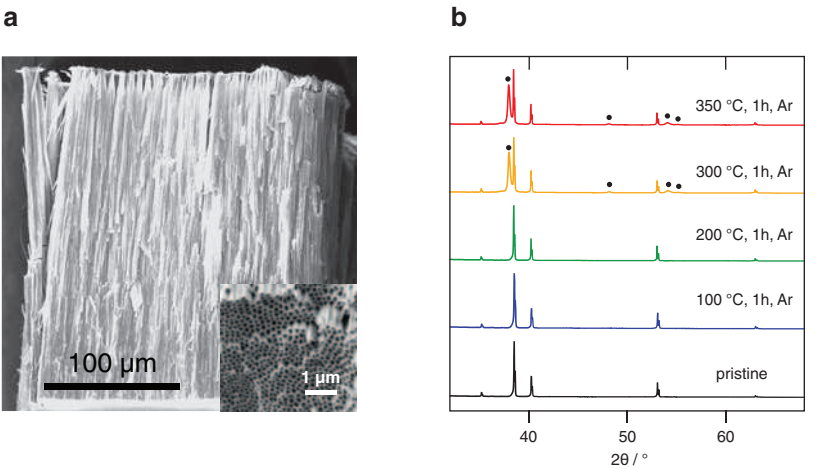

Fig. 2: (a) Cross section SEM micrograph of TiO_2 nanotube layer fabricated by anodization of Ti foil at 60 V for 5 days. The anodization bath consisted of ethylene glycol 97.6 wt%, water 2 wt%, NH_4F 0.4 wt%. The open end of the tubes is at the top of the picture while the closed end is at the bottom of the picture. The nanotubes are approximately 250 µm long and 130 nm in diameter with a wall thickness of 20–30 nm. The inset shows a detailed view of an intentionally broken section revealing the typical morphology of anodic titania nanotubes layers. (b) X-ray diffraction patterns of anodic TiO_2 nanotubes in pristine form and after annealing in Ar atmosphere. Up to 200 °C only the reflections of Ti metal substrate are visible. It is possible to convert the amorphous nanotubes to anatase (•) while keeping the morphology by annealing them in Ar or in air at 300–350 °C.

The typical morphology of the titania nanotube layers is shown in the inset of Figures 2a and 3b. The rather long tubes were used as anode material to prepare Li_xTiO_2 samples with the following compositions $x = 0.5$, $x = 0.75$ and $x = 1.0$.

Variable-temperature ^{7}Li NMR line shape measurements of these tubes revealed that Li ion diffusivity in the amorphous tubes is relatively slow. The rigid lattice line width, which is the line width at sufficiently low T where Li diffusivity has no effect on the NMR line shape, ranged from 12 to 16 kHz according to the amount of Li inserted per formula unit TiO_2. Motional narrowing of the NMR line sets in if Li ion hopping processes reach jump rates that are comparable with the rigid lattice line width. At sufficiently high T these exchange processes start to average homonuclear and heteronuclear dipole–dipole interactions that are responsible for the broadening of the spectra at low T. In the case of Li_xTiO_2 the Li^+–Ti^{3+} interaction leads to further broadening effects. For all compositions motional averaging is seen to take effect on the line shape at temperatures higher than 300 K. This is why so-called spin-alignment echo (SAE) NMR [44, 61–68] proved to be a suitable way to characterize Li ion diffusivity in the tubes prepared (Figure 2a). The method works in the regime where spin–spin-relaxation rates are still unaffected by motional averaging processes [65]. Here, the relatively poor ionic diffusivity as well as the coupling of the Li spins to paramagnetic centers like Ti^{3+} is reflected in a rigid-lattice relaxation time T_{20} of only 6 µs (see Figure 4a). An increase of T_2 is seen at temperatures higher than 330 K. Around this temperature and at $T > 300$ K the SAE NMR decay rates follow Arrhenius behavior with activation energies E_a ranging from 0.3 to 0.5 eV (see Figure 3a). Note that the data points referring to $x = 0.5$ and $x = 1.0$ were vertically shifted by 0.5 orders of magnitude each; the ^{7}Li SAE NMR rates do not significantly depend on composition at low T if rather large values of x are considered. In general, SAE NMR is sensitive to slow Li ion hopping processes ($<10^5$ 1/s) between electrically inequivalent Li sites. Usually the three-pulse sequence introduced by Jeener and Broekaert [61, 69–71] is used to measure a two-time correlation functions S_2 from which the decay rate $1/\tau_{SAE}(T)$ can be deduced.

Interestingly, above 400 K the decay rates from stimulated echo NMR start to decrease again. If T_2 is short enough this behavior can be traced back to averaging processes [61, 72] that occur during the mixing period; such a scenario has quite recently been discussed in detail for fast ion jump processes in Li bearing oxide garnets [73]. In these cases Li exchange processes may become too fast to be collected by SAE NMR. In the present case, however, we have to keep in mind the upper time window of SAE NMR, which is generally restricted by T_2; for comparison with $1/T_2$ the SAE NMR rates $1/\tau_{SAE}$ are jointly plotted with the spin–spin and spin–lattice relaxation rates of $Li_{0.75}TiO_2$ in Figure 4a.

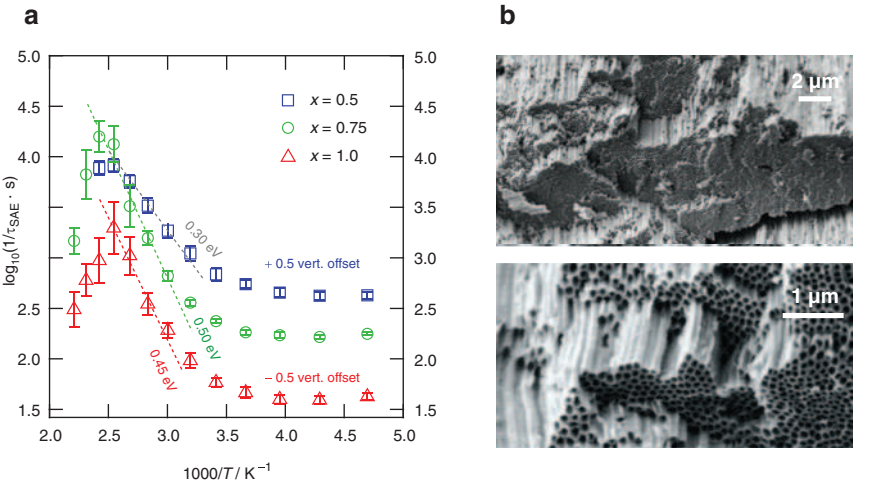

Fig. 3: (a) ^{7}Li NMR spin-alignment echo decay rates (194 MHz) vs. the inverse temperature of various Li_xTiO_2 samples that were prepared electrochemically. To record the rates, two-time correlation functions were measured at constant preparation time (20 µs) but variable mixing-time utilizing the three-pulse sequence by Jeener and Broekaert. (b) SEM images revealing the morphology of the tubes investigated by Li NMR.

Interestingly, for the samples with $x > 0.5$ we observed quite high activation energies by SAE NMR. Values a large as 0.5 eV are in good agreement with those reported for crystalline Li_xTiO_2-B nanowires. Similarly, for mixed-conducting $Li_{1.0}TiO_2$, which was prepared by chemical lithiation, an activation energy of 0.58 eV was obtained (see Figure 4b). While SAE NMR is sensitive to slow Li^+ exchange processes, which in many cases reflect long-range ion transport also accessible by DC conductivity measurements [63], SLR NMR is sensitive to more localized, short-range ion movements [29, 74, 75]. As expected, if the low-T regime of a given $1/T_1(1/T)$ rate peak is considered, much lower activation energies were probed through laboratory-frame ^{7}Li SLR NMR [74, 75]. For $Li_{1.0}TiO_2$ we were able to reach the beginning of the low-T flank of the diffusion-induced $1/T_1(1/T)$ rate peak which resulted in 0.15 eV. Note that this flank was masked in the case of the electrochemically lithiated samples. Presumably, it was hidden by an increased Li–electron contribution to the overall spin–lattice relaxation rate. The electrochemically prepared samples are expected to contain minute amounts of fluorine from anodization. This F content will increase the electronic conductivity of the samples. As a result, coupling of the spins with conduction electrons shortens the overall T_1 relaxation time which narrows the time window of time-domain NMR measurements. In extreme cases the diffusion-induced contributions to the overall spin–lattice relaxation rates are completely masked [45]. In particular, due to the large volume fraction

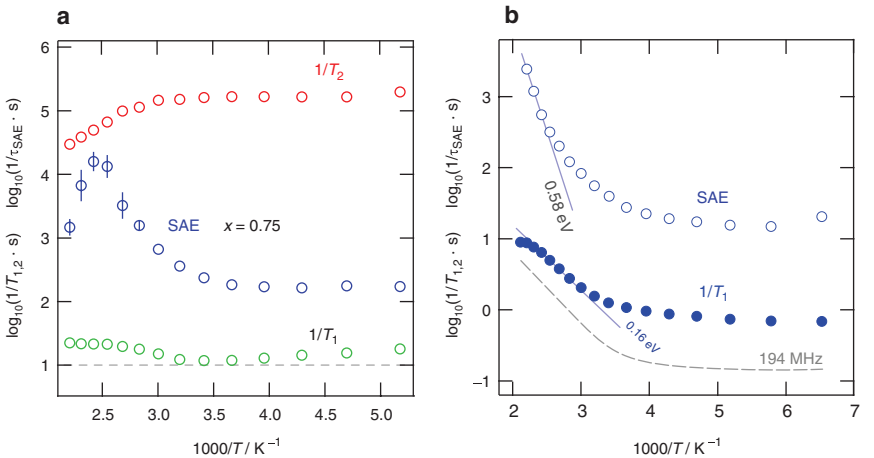

Fig. 4: (a) Temperature dependence of the (i) ^{7}Li SAE NMR decay rates, the (ii) ^{7}Li NMR spin–lattice and the (iii) spin–spin relaxation rates of $Li_{0.75}TiO_2$ (116 MHz). While $1/T_1$ suffers from Li^+–Ti^{3+} interactions as well as the influence of additives such as binders and conductive agents of the electrode resulting in short T_1 times of <1 s, SAE NMR is able to recognize a diffusion-induced increase at $T > 330$ K. The shallow increase of $1/T_1$ at low T can be ascribed to Curie–Weiss behavior. (b) ^{7}Li SAE NMR response of $Li_{1.0}TiO_2$ that was prepared by chemical lithiation of the amorphous titanate nanotubes. As compared to the electrochemically lithiated samples, the absolute, non-diffusive rate $1/T_1$ is lower which allowed us to measure the beginning of a diffusion-induced $1/T_1(1/T)$ rate peak. The curvature seen at high T most likely reflects a local rate maximum which would be in accordance with the low activation energy probed (0.15 eV). At the same temperature (ca. 500 K) SAE NMR points to quite slow Li exchange processes that characterize long-range ion transport with 0.58 eV.

of interfacial regions of nanocrystalline TiO_2 the spin–electron interactions with conductive carbon additives in contact with these surface regions can drastically shorten the T_1 times, which also restricts the applicability of other NMR techniques that are limited by T_1 such as rotating-frame SLR measurements (*vide infra*).

2.1.2 Crystalline TiO_2 nanotubes crystallizing with the anatase structure

As noted above, the amorphous titania nanotubes convert into anatase at elevated T. Alternatively, anatase nanotubes can be prepared following a hydrothermal route. In Figure 5 the high-resolution (HR) transmission electron microscopy (TEM) images of hydrothermally synthesized nanocrystalline TiO_2 tubes are shown. X-ray powder diffraction and ^{7}Li NMR spectroscopy point to a highly crystalline material whose tubes crystallize with the anatase structure (Figure 6). By varying the

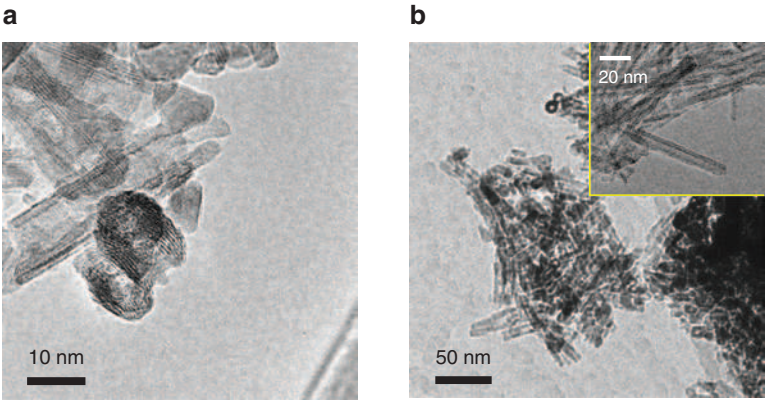

Fig. 5: (a) and (b) HR TEM images of anatase nanotubes prepared hydrothermally. The average length of the tubes is ca. 50 nm. The diameter ranges from 10 to 12 nm. After exchanging the Na^+ ions in the initially formed sodium titanate $Na_{2-x}H_xTi_nO_{2n-1} \cdot yH_2O$ with H^+ the final calcination step yields TiO_2 nanotubes.

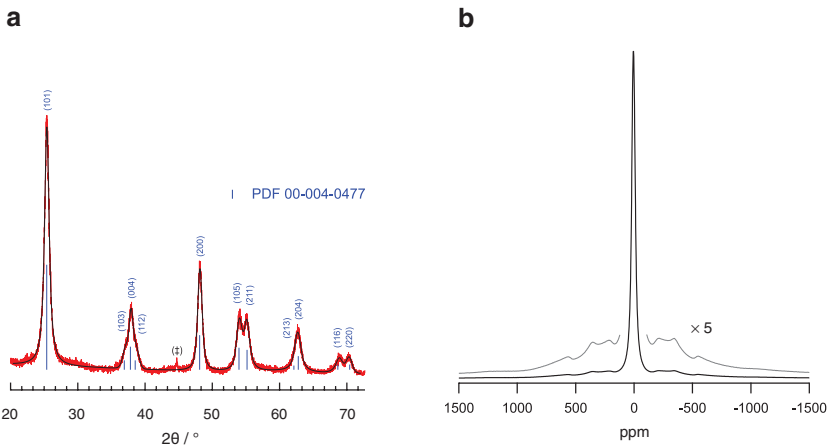

Fig. 6: (a) X-ray powder diffractogram of the nanotubes prepared via hydrothermal synthesis. The Miller indices reflect those of anatase; vertical bars reflect positions and intensities expected for anatase, see the PDF indicated. Strongly broadened reflections reveal a crystalline sample with nm-sized crystallites as could be verified via HR TEM. (b) ^{7}Li NMR spectrum recorded under static conditions (116 MHz). Besides the central transition, the distinct quadrupole powder pattern illustrates the crystallinity of the sample as is also evidenced by the HR TEM images taken.

synthesis conditions, e.g. the synthesis temperature, the molarity of the sodium hydroxide solution, the pH-value during the washing procedure or the temperature while calcination, either anatase or TiO_2-B nanotubes can be obtained. If used

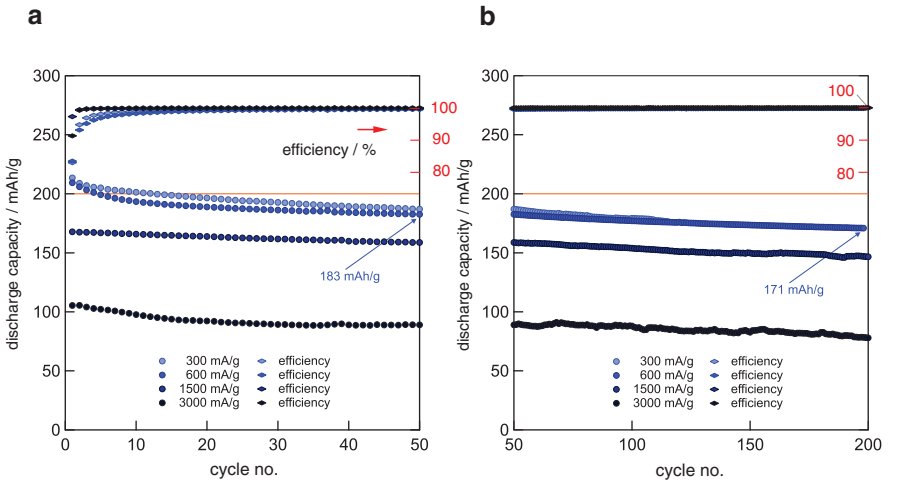

Fig. 7: (a) and (b) Discharge capacities of TiO_2 nanotubes crystallizing with the anatase structure. In (a) the first 50 cycles are shown. The currents indicated correspond to C-rates of 1.5 C (300 mA/g) and 15 C (3000 mA/g), respectively. At 1.5 C capacities in the order of 170 mAh/g are reachable even after 200 full cycles. Coulomb efficiencies are close to 100 %.

as negative electrode material in lithium half cells the anatase tubes show excellent cycling behaviour. At C-rates of 1.5 C a relatively stable discharge capacity of 170 mAh/g is reached (see Figure 7); only a small capacity fade is seen with increasing cycle number. Even after 200 full cycles the Coulomb efficiency is close to 100 %.

To shed light on Li ion dynamics of TiO_2 nanotubes, which were either treated with *n*-BuLi or lithiated electrochemically in Li half cells, we recorded ^{7}Li NMR line shapes and spin–lattice relaxation rates. As an example, in Figure 8 the rates $1/T_1$ and $1/T_{1\rho}$ of $Li_{0.6}TiO_2$ (TiO_2-B) are shown. Li was inserted electrochemically using Swagelok cells; the final electrode contained 15 wt% binder (Kynar Flex 2801) and conducting additives [carbon black 15 wt% (Super P)].

Whereas for $Li_{0.6}TiO_2$ the rate $1/T_1$ only weakly depends on temperature, for the anatase tubes with $x = 0.3$ and $x \approx 0.13$, which were chemically lithiated, $1/T_1$ reveals the shallow flank of a $1/T_1(1/T)$ rate peak that is characterized by ca. 0.15 eV. Most likely, for Li_xTiO_2 such a low activation energy has to be assigned to localized relaxation processes rather than to long-range ion transport. Li ions near the surface regions are expected to be involved in such processes. In all cases and irrespective of the final crystal structure of the titania nanotubes the corresponding spin-lock NMR transients, from which we extracted the rates $1/T_{1\rho}$, obey a rather complex behavior. At sufficiently high x values ($x > 0.1$) we clearly observed a two-step decay behavior.

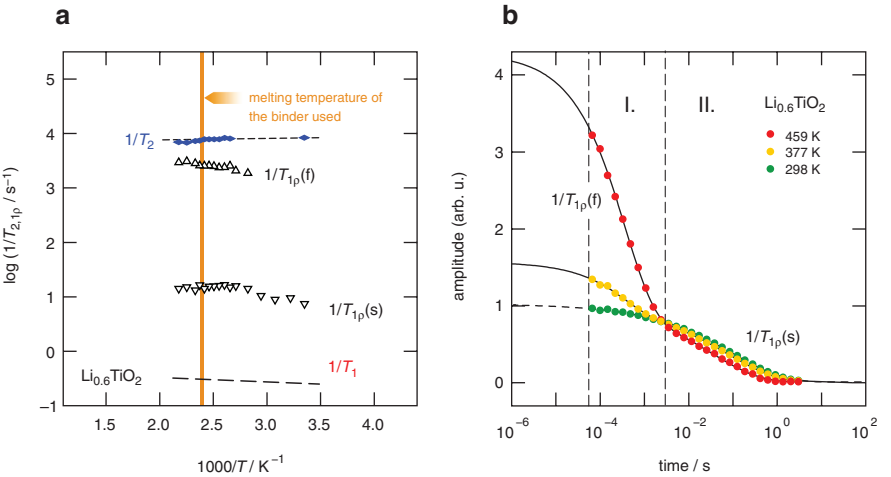

Fig. 8: (a) ^{7}Li NMR spin–spin ($1/T_2$) and spin–lattice relaxation rates ($1/T_{1(\rho)}$) of $Li_{0.6}TiO_2$ (TiO_2-B) nanotubes recorded at a Larmor frequency of 116 MHz. The corresponding spin-lock rates were acquired at a locking frequency of 20 kHz. The dashed line indicates the temperature dependence of the laboratory-frame rates $1/T_1$. Note that the binder used to prepare the electrodes for electrochemical lithiation melts at ca. 415 K, see the vertically drawn line. Above 330 K, for $1/T_{1\rho}$ two rates, marked with (s) and (f), were obtained that significantly differ from each other. The rate $1/T_{1\rho}$(s) could be largely influenced by spin-diffusion effects. The rate $1/T_{1\rho}$(f) might represent a subset of fast Li ions near the interfacial regions of the TiO_2-B nanotubes. (b) Transversal $T_{1\rho}$ magnetization transients (20 kHz) revealing the two sub-transients from which the rates $1/T_{1\rho}$(s) and $1/T_{1\rho}$(f) were extracted. Dashed and solid lines represent fits with a sum of two stretched exponentials. With increasing T the fast decaying contribution emerges (region I.); at 459 K the ratio of the amplitudes of the two signals is 3:1. Thus, the majority of the Li ions, possibly those near the surface regions, has access to a fast spin-lock decay. According to this preliminary explanation, the tail of the overall transients (region II.) should then represent those ions residing in the inner regions of the walls.

This behavior is exemplarily shown for the $Li_{0.6}TiO_2$-B in Figure 8b. Parameterizing the transients with a sum of two (stretched) exponentials results in the rates $1/T_{1\rho}$(s) and $1/T_{1\rho}$(f). The two-step behavior cannot be explained by the spin-properties of the ^{7}Li nucleus as their difference greatly exceeds that usually expected for, e.g. quadrupolar relaxation. While $1/T_{1\rho}$(f) is close to $1/T_2$, independently measured through spin-echo experiments, the rate $1/T_{1\rho}$(s) is in the order of seconds. A significant temperature dependence is obviously masked because of, e.g. Li^{+}–Ti^{3+} interactions, spin-diffusion, surface effects or the presence of a variety of (nm-sized) crystalline regions that differ, e.g. in Li content. The magnitude of $1/T_{1\rho}$(s) and its temperature independence resembles that expected for spin-diffusion that is, e.g. mediated through a spatially homogenous distribution

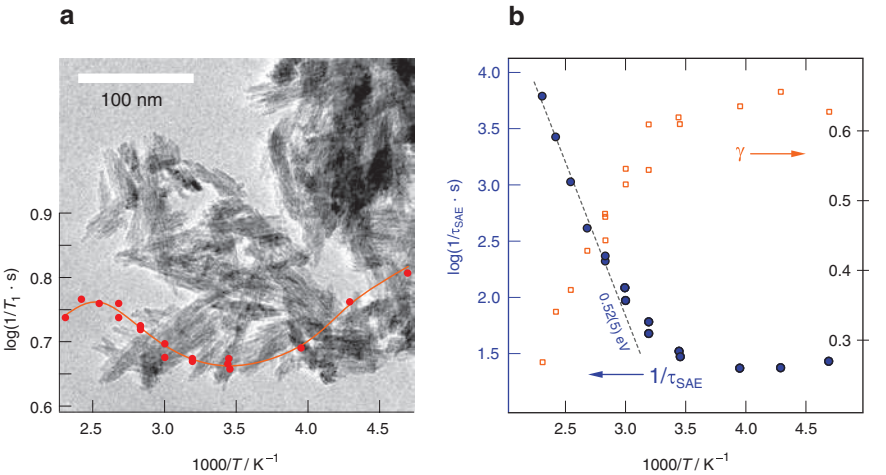

Fig. 9: (a) SEM image of TiO_2 (rutile) nanorods; the needlelike shape of the crystallites is clearly visible. X-ray diffraction confirmed the phase purity of the material. The data points at the bottom of the figure illustrate the temperature dependence of the T_1 relaxation rates measured at a Larmor frequency of 116 MHz. (b) ^{7}Li SAE NMR decay rates of $Li_{0.5}TiO_2$ (rutile); for comparison, the stretching exponents used to parameterize the underlying S_2 decay curves are also shown.

of paramagnetic centers such as Ti^{3+}. The NMR line shapes of all samples investigated point to very slow ion dynamics which is in line with the observations for amorphous titania nanotubes. Additional ^{7}Li SAE NMR measurements are currently running in our labs to shed light on the origins of the two Li sub-ensembles seen in spin-lock NMR.

2.1.3 Li diffusion in rutile nanorods and their electrochemical behaviour

Slow Li ion diffusion was also found for nanostructured rutile whose electrochemical performance in Li-ion cells is comparable to that of the TiO_2 nanotubes investigated. We studied both the cycling behaviour and the Li ion diffusivity of needlelike Li_xTiO_2 crystallizing with the rutile structure. The powder used for the experiments was a commercial one that is characterized by small needles, ca. 40 nm in length and 10 nm in diameter, see Figures 9a and 10a. Earlier ^{7}Li NMR spin–lattice relaxation and SAE measurements (see Figures 9 and 10) were performed on a sample with $x = 0.5$ that was chemically lithiated by treatment in *n*-BuLi dissolved in hexane [76]. SEM images and X-ray powder diffraction of the highly air-sensitive product confirmed that the rutile structure is fully retained

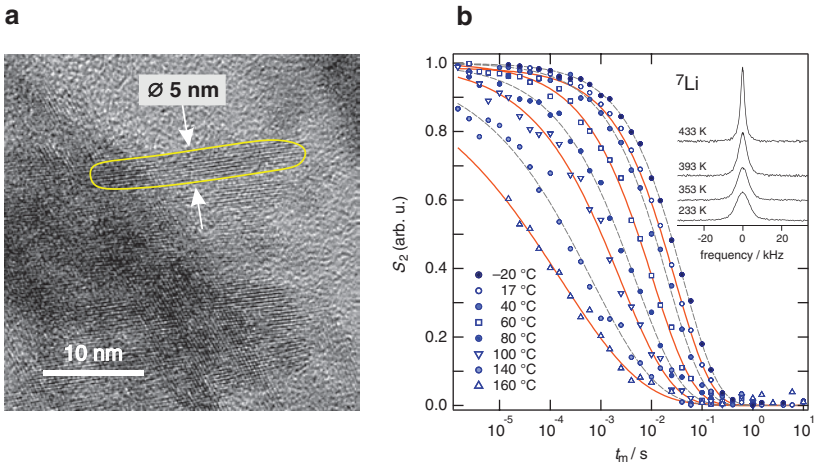

Fig. 10: (a) HR TEM image of the rutile nanorods investigated; a nanorod with a length of ca. 25 nm and a diameter of approximately 5 nm is highlighted. (b) ^{7}Li SAE NMR S_2 decay curves (78 MHz) recorded at a preparation time of 10 µs. The curves were approximated with stretched exponentials; the corresponding stretching factors are shown in Figure 9b; they range from 0.3 to 0.7 clearly representing a non-exponential motional correlation function. Inset: ^{7}Li NMR lines recorded at the temperatures indicated. The lines show a Gaussian shape at low T and transform into a Lorentzian line at elevated T.

during Li insertion. This contrasts with other modifications of TiO_2 for which lithiation is accompanied with a phase transformation. For rutile such transformations are reported for samples with $x > 0.5$.

As in the case of amorphous TiO_2 nanotubes we took advantage of ^{7}Li SAE NMR to characterize Li ion hopping in rutile $Li_{0.5}TiO_2$. Most interestingly, also for nanocrystalline, rutile $Li_{0.5}TiO_2$ the decay rates $1/\tau_{SAE}$ are governed by non-diffusive effects until ca. 310 K. At higher T they discharge into an Arrhenius line that is once again characterized by an activation energy in the order of 0.5 eV. Significant motional line narrowing is recognized at 300–350 K (see inset of Figure 10b), thus at slightly higher temperatures than it was the case for amorphous TiO_2 indicating faster ion dynamics in the structurally disordered samples. Note that for amorphous $Li_{0.5}TiO_2$ the activation energy derived from SAE NMR was only 0.3 eV. As also observed for the amorphous samples, the SAE NMR decay curves S_2 could only be parameterized with stretched exponentials $S_2 \propto \exp(-(t_m/\tau_{SAE})^\gamma)$, see Figure 10b. The beginning of the diffusion-controlled SAE NMR flank is associated with the beginning of the decrease of the exponent γ ($0 < \gamma \leq 1$) that describes the deviation from single-exponential time behavior $\gamma = 1$. This behavior is generally observed in SAE NMR if materials with a (large) distribution of decay rates are considered.

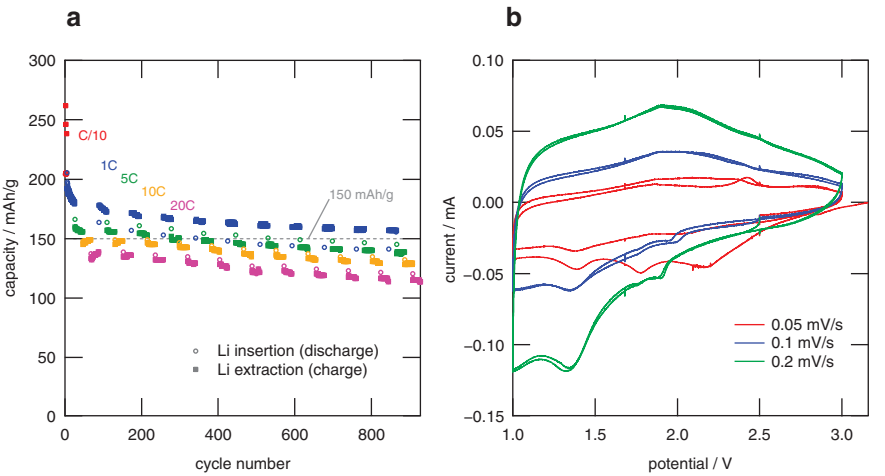

Fig. 11: (a) Discharge/charge capacities of the rutile nanorods if tested in Li half cells at various C-rates ranging from C/10 to 20C. At 1C the capacities are well above 150 mAh/g, thus comparable with those of the anatase nanotubes hydrothermally prepared. (b) Cyclic voltammograms of the Li ion cells equipped with the rutile nanorods.

Despite the moderate to poor ion dynamics in rutile $Li_{0.5}TiO_2$ the nm-sized needles perform exceptionally well in lithium-ion cells; therefore, one might speculate whether surface and interface effects do significantly participate in facile Li storage. To test their electrochemical ability to work as anode material in cells (with Li metal as both counter and reference electrode) we prepared electrodes consisting of nano-$Li_{0.5}TiO_2$, binder (Kynar Flex 2801) and carbon powder (Super C 65); the weight ratio was 75:17:8. The cyclic voltammograms reveal a distribution of various redox processes (Figure 11b), at a scanning rate of 0.05 mV/s three distinct peaks are visible that indicate distinct insertion/de-insertion processes presumably associated with structural changes of the active material if electrochemically lithiated. Galvanostatic cycling at current rates ranging from 0.1 C to 20 C proves a credible rate capability (Figure 11a). For instance, at 1 C the decrease in charge capacity turned out to be marginal; even after 800 cycles the cell delivers a stable discharge capacity of more than 150 mAh/g.

2.1.4 Mesoporous TiO_2 as long-lasting anode material

Mesoporous materials with an ordered 3D pore structure ensure superior storage capacities and facile Li insertion and removal. As mentioned above, these

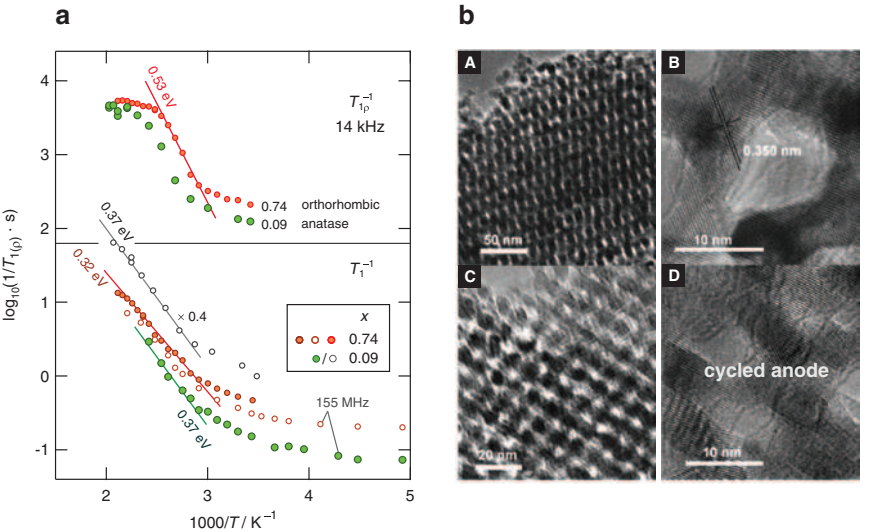

Fig. 12: (a) ^{7}Li NMR spin–lattice relaxation rates of mesoporous Li_xTiO_2 with $x = 0.09$ and $x = 0.74$, see Ref. [43]. The rates were recorded at 78 MHz and 155 MHz. For the sake of clarity, the data of $Li_{0.09}TiO_2$ (78 MHz) were vertically shifted by a factor of 4. In the upper graph of (a) the spin-lock rates are shown that were acquired at a locking frequency of 14 kHz. (b) High-resolution TEM images revealing the pore structure of the material before (A and B) and after cycling (C and D). No significant changes can be seen ensuring a high morphological stability of the mesoporous anode. TEM images taken from Ref. [39], copyright © 2000 by John Wiley Sons, Inc. Reprinted by permission of John Wiley & Sons, Inc.

properties are *inter alia* related to short diffusion lengths of the nm-sized materials [35] as well as, see the discussion above, to the involvement of Li surface storage. Because of the large volume fraction of the interfacial regions this storage mechanism needs to be considered. Recently, excellent cycling behavior of a lithium-ion battery was achieved when mesoporous TiO_2 with a 3D hierarchical pore structure was used as anode material [39]. Even after extensive charging and discharging of the battery, the hierarchical pore structure was preserved throughout clearly illustrating the high stability of the anode, see the HR TEM images in Figure 12b that were taken from Ref. [39].

Initially, the mesoporous TiO_2 crystallizes with tetragonal symmetry. Upon Li insertion the material transforms, however, into an orthorhombic form [39]. Besides kinetic effects also Li diffusion properties are anticipated to govern the insertion and removal rates. To answer the important question if and to which extent Li self-diffusion changes as a function of Li content x in mesoporous Li_xTiO_2, we used ^{7}Li NMR relaxometry and ^{7}Li SAE NMR to probe local activation energies and jump rates [43]. As mentioned above, while ^{7}Li SAE NMR is useful

to probe rather slow Li motions with correlation rates lower than 10^5 Hz, ^{7}Li NMR SLR measurements, in both the laboratory and rotating frame of reference are applicable to detect hopping processes with rates ranging from 10^5 Hz to 10^9 Hz [74, 75, 77]. Owing to the relatively long ^{7}Li NMR SLR rates of the samples in the rigid-lattice regime, we could detect the low-T flanks of the corresponding rate peaks. The key results are shown in Figures 3 and 4.

In Figure 12a ^{7}Li NMR spin–lattice relaxation rates for two compositions x, i.e. two crystal structures, are shown that were recorded at 155 MHz and 78 MHz as well at a locking frequency of 14 kHz. The Arrhenius plot reveals that above 300 K the rates start to be mainly governed by ionic diffusion processes. Below that temperature non-diffusive origins control the rates. As expected, the more Ti^{3+} centers have been generated through the insertion of Li^+/e^- the larger the paramagnetic Li^+–Ti^{3+} spin–spin interaction and the faster the longitudinal recovery in the low-T regime.

In the laboratory frame the diffusion-controlled rates follow Arrhenius behaviour that points to activation energies, E_a, of 0.37 eV ($x = 0.09$) and 0.32 eV ($x = 0.74$), respectively. Both the decrease in E_a and the slight increase in absolute values in the diffusion-induced regime indicate increased Li ion hopping processes in the sample with higher Li content. This view is supported by spin-lock NMR, see the upper part of Figure 12a. At first glance, one would expect a decrease in Li ion diffusivity if x is significantly increased from 0.09 to 0.74. Such a decrease could be the result of large Coulomb interactions at high x values with many interfering Li ions and a restricted number of vacant Li sites. The experimental results, however, point to the opposite direction: the dynamic parameters deduced from NMR turned out to be less influenced by the Li content than expected. If we consider surface effects and the fact that the crystal symmetry reversibly changes from tetragonal to orthorhombic when going from $x = 0.09$–0.74 some solid arguments can be found being able to explain the current NMR response. The orthorhombic structure seems to facilitate Li ion migration which, on the other hand, is highly beneficial for the performance of the anode material that needs to easily accept and conduct Li ions at increased values of x.

The fact that Li bulk diffusivity is seen to increase rather than to decrease with increasing x in mesoporous Li_xTiO_2 is also underpinned by ^{7}Li SAE NMR measurements, Figure 13, see Ref. [43]. Also from the point of view of SAE NMR correlation rates, the gradual transformation into orthorhombic Li_xTiO_2 upon Li insertion, i.e. during charging the anode in a battery with full cell configuration, seems to have a positive effect on Li ion diffusivity (see Figure 12a and b).

By parameterizing the SAE decay curves, exemplarily shown in Figure 13a for $x = 0.09$, we obtain temperature-dependent correlation rates $1/\tau_{SAE}$ that start to be influenced by slow Li exchange processes at temperatures above 250 K. By careful

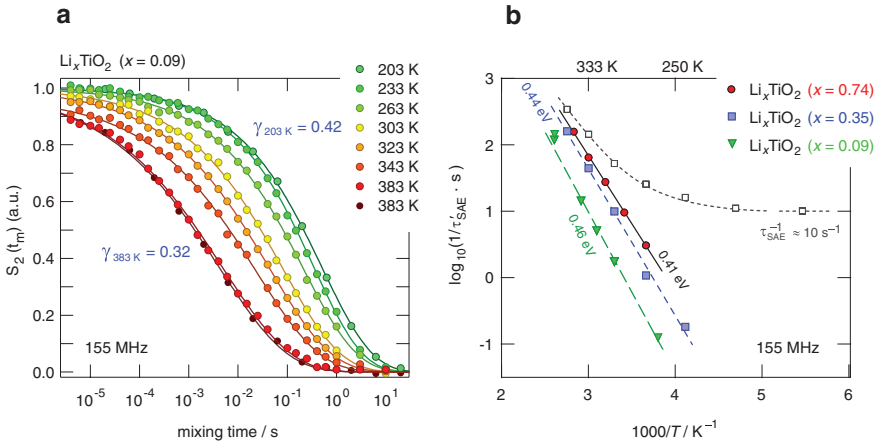

Fig. 13: (a) ^{7}Li NMR two-time (sin–sin) correlation functions recorded at 155 MHz with the Jeener–Broekaert three-pulse sequence to generate stimulated echoes. The amplitude of the echo generated after the reading pulse is plotted as a function of mixing time, t_m, while the preparation time t_p was kept constant (10 μs). The shape of the decay curves do only slightly depend on T; the solid lines show fits with stretched exponentials. For $x = 0.09$ the stretching exponents γ vary from 0.3 to 0.45 indicating correlated motion and/or a relatively wide distribution of motional correlation times. The corresponding decay rates are shown in (b). With increasing x a slight increase rather than a decrease in SAE NMR decay rate is found that corroborates the findings from spin-lock NMR. Figures adapted from Ref. [43].

subtraction of the almost temperature-independent and non-diffusive contributions to the SAE decay from the overall rates we ended up with purely diffusion-controlled rates $1/\tau'_{SAE}$ that follow Arrhenius-type behaviour. The straight lines in Figure 13b represent Arrhenius fits with activation energies of 0.48 eV ($x = 0.09$), 0.44 eV ($x = 0.35$), and 0.41 eV ($x = 0.74$). These values are comparable with those from NMR relaxometry. They are higher than those from SLR NMR in the lab frame since laboratory-frame relaxation is able to gather also short-ranged (local) ion dynamics to which SAE NMR is less sensitive.

On the other hand, SAE NMR, although being able to characterize long-range ion transport, is insensitive to ion jump processes between electrically identic sites that albeit contribute to NMR relaxometry, e.g. in the rotating frame of reference. This fact might explain the higher activation energy seen via spin-lock NMR which obviously also probes ion hopping processes with even larger barriers the ions have to surmount (0.53 eV for the sample with $x = 0.74$). It is, on the other hand, important to mention that the temperature ranges where the two techniques have been applied to measure ion dynamics do not coincide. Above 383 K the SAE decay curves start to be independent of temperature. Thus, at high

temperatures, i.e. in the regime of 'fast' ion dynamics, SAE NMR is unable to produce reliable jump rates and activation energies.

A similar feature can be seen for the spin-lock rates of the sample with $x = 0.74$. At high T, the rates follow an anomalous T behaviour that needs to be investigated in future studies. We suppose that it is related to the, to some extent irreversible, interaction of the active material with binders and carbon additives that are usually added to 'ionically' and electronically activate TiO_2 to prepare a functioning battery anode. Nevertheless, in the T range of battery operation we have seen that at increased values of x the orthorhombic form of mesoporous TiO_2 with its hierarchical pore structure represents a powerful anode material with slightly enhanced Li ion dynamics compared to the initially Li poor TiO_2 with tetragonal symmetry.

2.1.5 Na insertion into amorphous TiO_2 nanotubes: mechanistic details – differences between Li and Na

While the electrochemical reactions of nanostructured TiO_2 with H^+ and Li^+ have been known for a while, the particularities of the electrochemical reaction of Na^+ with anodic titania nanotubes are a more recent achievement. A cyclic voltammetry experiment investigating the Na^+ insertion into amorphous TiO_2 nanotubes (see Figure 14a) does not indicate a definite two-phase insertion mechanism as known for insertion of Li^+ in crystalline forms of titania [42]. A 2-phase mechanism would result in well-defined current peaks in the cyclic voltammogram. The very broad current response, however, hints to a one-phase mechanism that might instead be involved. Another feature is the relatively symmetrical response of the nanotubes with respect to Na^+ electrochemical reaction when the sweep rate is increased, e.g. at 10 mV/s, contrasting with the asymmetric shape of the cyclic voltammogram recorded at relatively slow seep rates of, e.g. 0.5 mV/s.

In Figure 14b the current read at 1 V vs. Na^+/Na has been plotted against the square root of the sweep rate for three different types of amorphous anodic titania nanotubes, see Ref. [42]. Obviously, the nanotubes possess different outer diameters and lengths as follows: after anodization at 30 V for 2 h the nanotubes length was approximately 4.5 μm and 70 nm in diameter, at 40 V after 2 h 8 μm and 100 nm while at 50 V after 1 h the tubes were 9.1 μm long and 120 nm in diameter. For an electrochemical process limited by a mass transport phenomenon a Randles–Ševčík-type plot, as presented in Figure 14b, should be linear. However, even after any ohmic drops were eliminated, there is a clear deviation from this expected linearity. The deviation is always positive, i.e. the current is higher than expected. Moreover, the deviation magnitude increases with sweep rate. This

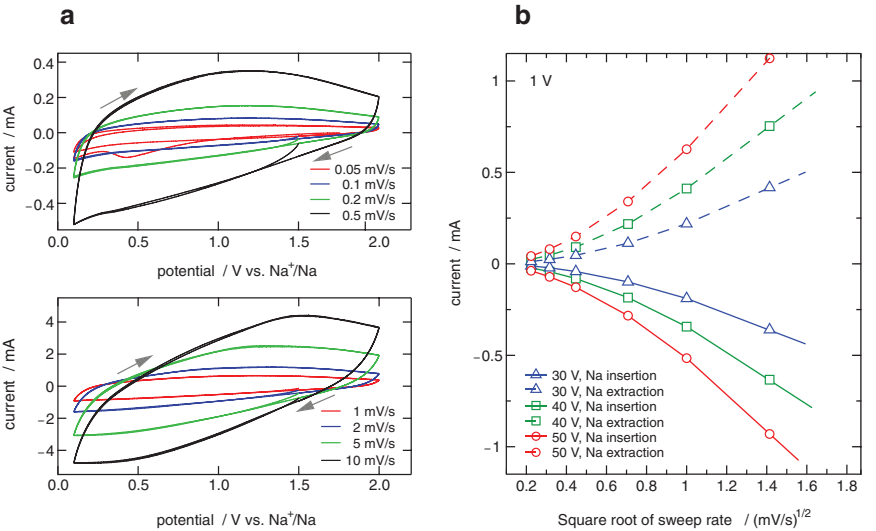

Fig. 14: (a) Cyclic voltammetry response at various sweep rates of an amorphous TiO_2 nanotubes layer fabricated by anodization at 50 V for 2 h. The electrolyte was solution of 1 M $NaClO_4$ in propylene carbonate (PC). The electrochemical response of the sample is consistent with a sodium storage mechanism involving a single phase mechanism. (b) The current values read from a) at a potential of 1 V vs. Na^+/Na plotted with respect to square root of the sweep rate of the anodic and cathodic scans. There are significant and systematic deviations from the linear behaviour that would be expected for electrochemical processes that are limited by mass transport (diffusion) phenomena. Figures adapted from Ref. [42].

observation proves that there is a process, contributing to Na^+ storage, which is faster than solid-state diffusion in the walls of TiO_2 nanotubes. This contributing process is commonly called pseudo-capacitive storage. Although a charge transfer takes place and a Ti^{4+} redox center is reduced to Ti^{3+} during electrochemical reaction with sodium, the corresponding Na^+ ion does not diffuse into the bulk of the amorphous titania material. Instead, it adsorbs onto the titania/electrolyte interface region forming a somehow loose bound with the substrate while still compensating the negative charge of the mobile electron that has been injected into TiO_2 conduction band. This interfacial storage mechanism is obviously not limited by ion diffusion in the solid-state since the Na^+ ions reside on the surface of the material. The only mass transport limitation by diffusion occurs in the liquid state, i.e. chemical diffusion of the sodium species through the liquid electrolyte. Chemical diffusion in the liquid state can, however, safely be considered at least 4–6 orders of magnitude faster than the solid-state diffusion process and, thus, this process is significantly faster than its solid-state counterpart, as is clearly proven by the non-linear relationship observed in Figure 14b.

It is possible to separate the pseudo-capacitive and chemical diffusion process in the solid state by considering that diffusion should present a linear response on a Randles–Ševčík-type plot and that the pseudo-capacitive contribution adds to the diffusion process while being non-linear with respect to the sweep rate. By a relatively simple subtraction technique, detailed elsewhere [42], we found very high values of the pseudo-capacitance as shown in Figure 15a. The pseudo-capacitance is increasing as the potential of the electrode is driven towards more negative values, eventually reaching very high values around 1000 μF/cm^2. Worth mentioning, this value is roughly two orders of magnitude higher than the usual double layer capacitance occurring in the absence of a faradaic process. This opens the path towards the use of anodic titania nanotubes in supercapacitors. While the pseudo-capacitive contribution of the anodic titania is very high, the Na^+ diffusion into the walls of the nanotubes is very slow irrespective of the electrode potential at which it was measured as seen in Figure 15b. The chemical diffusion coefficient values are centered around 10^{-21} cm^2/s which is 4–5 orders of magnitude lower than the corresponding Li^+ diffusion coefficients in anatase TiO_2 [78]. Therefore, there is

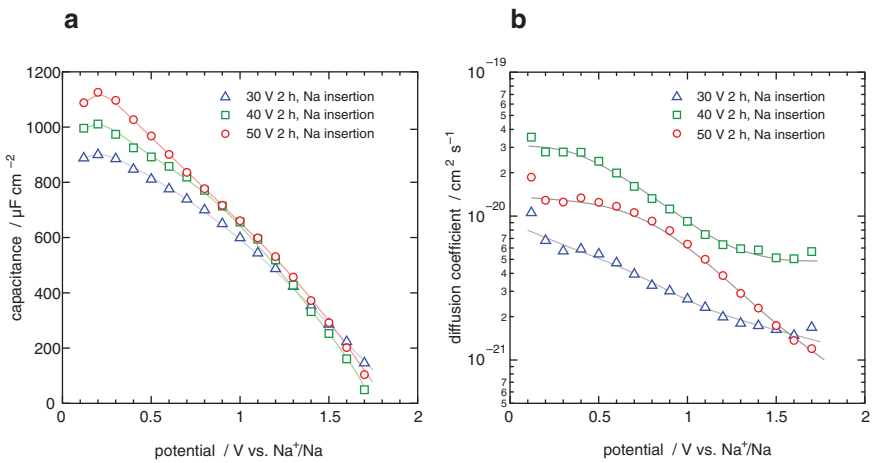

Fig. 15: (a) The pseudo-capacitive Na^+ interfacial storage for TiO_2 nanotubes with respect to the electrode potential. The values of the capacitance are expressed with respect to the surface area of the nanotubes that is much higher than the surface occupied by the nanotubes layer on the Ti substrate. For these samples this surface ratio lies between 450 and 700:1. (b) Chemical diffusion coefficient corresponding to sodium insertion in the walls of the TiO_2 nanotubes; values were determined after subtraction of the pseudo-capacitive contribution. Regardless of the potential of the electrode, diffusion of sodium into TiO_2 turned out to be rather slow process at room temperature. Figures adapted from Ref. [42].

only a small amount of sodium diffusing into the walls of the titania nanotubes, most of the sodium storage capacity originates from the pseudo-capacitive processes. This feature is essentially different from Li^+ insertion in TiO_2, most of the Li^+ is actually stored in the bulk regions of TiO_2 below a certain electrode potential, typically lower than 1.5–1.7 V vs. Li^+/Li.

2.2 Li ion diffusion in layer-structured (nanocrystalline) Li_xSnS_2 with confined Li diffusion pathways

Macroscopic Li diffusion in nanostructured ceramics, such as TiO_2, can be directed if the crystallites assume the shapes of tubes or rods. From the atomic scale point of view the elementary hopping processes have to be characterized in many cases by 3D diffusion unless diffusion of the ions is preferred along a special direction of the crystal structure. Apart from such anisotropic movements in materials offering 3D diffusion there are layer-structured and channel-structured ion conductors with significantly constraint migration pathways [30, 65, 79–84]. Lithium transition metal dichalcogenides represent a typical class of materials that offer 2D diffusion in their van-der-Waals gaps [83]. Of course, besides intralayer diffusion, to a minor extent also interlayer hopping processes across the layers can take place. Considering sulfides, besides, e.g. Li_xTiS_2 [62, 83] and Li_xNbS_2 [81, 85], the Sn-analogue, Li_xSnS_2, constitutes another interesting model system not only to study the influence of dimensionality [49] but also the effect of structural disorder on a spatially confined diffusion process.

In Figure 16a ^7Li NMR spin–lattice relaxation rates of three different Li_xSnS_2 ($x = 0.17$) samples, differing in morphology and mean crystallite size, are shown in an Arrhenius plot. With $x = 0.17$ we ensured that mainly intralayer Li sites, i.e. those between the SnS_2 sheets, have been occupied by the Li ions. The mobile Li ions were chemically introduced into SnS_2 via treatment with *n*-BuLi in hexane. Microcrystalline Li_xSnS_2 served as reference material to reveal the changes in diffusion-induced NMR spin-lock relaxation rates [49]. NMR spin–lattice relaxation in $Li_{0.17}SnS_2$ with µm-sized crystallites turned out to be rather complex. We interpreted the appearance of two diffusion-induced rate peaks as a consequence of a heterogeneous distribution of Li ions in Li_xSnS_2 that can be influenced by annealing [49]. Soft thermal treatment is anticipated to homogenize the sample toward a uniform distribution of intercalants [81]. After thermal annealing the low-*T* peak 1 (see Figure 16b) has significantly been decreased in intensity. We assume that this relaxation peak represents clustered Li ions near the surface-influenced regions having access to fast short-range motions.

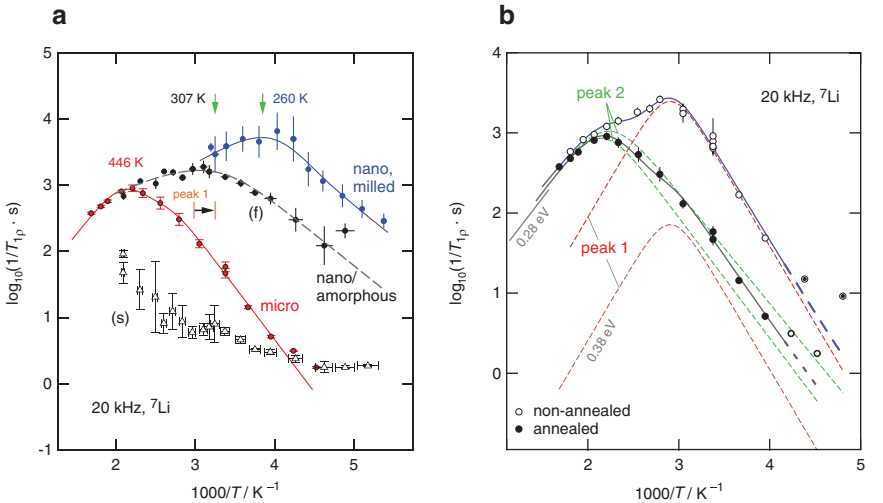

Fig. 16: (a) ^{7}Li NMR spin–lattice relaxation rates of different $Li_{0.17}SnS_2$ samples: a microcrystalline one (see red data points), a nanocrystalline one with a large fraction of amorphous material, and a sample that was prepared mechanochemically from Li_2S and SnS_2 in a planetary mill. The rates were recorded at a locking frequency of 20 kHz. (b) The diffusion-induced NMR locking rates of microcrystalline $Li_{0.17}SnS_2$ before (unfilled symbols) and after annealing the sample (filled symbols). In both cases the data can be best represented by two diffusion-induced rate peaks pointing to two dynamically distinct motional processes. Figure (b) adapted from Ref. [49].

If a nanocrystalline sample is studied that contains large volume fractions of amorphous Li_xSnS_2 the NMR response clearly differs from that found for microcrystalline Li_xSnS_2. At first the corresponding NMR line shapes of the nanocrystalline sample are composed of two contributions with quite different line widths (Figure 17). Thus, we have indeed to deal with a sample consisting of two spin reservoirs largely differing in ion dynamics, see also Ref. [33]. The sharp line resembles that of microcrystalline $Li_{0.17}SnS_2$; most likely, the ions representing this line reflect those in the nanocrystalline grains. The broader line can then be assigned to those in the amorphous regions. The two spin ensembles are also visible in ^{7}Li NMR spin-lock NMR transients which can only be parameterized with a sum of two single transients. The resulting rates are denoted as (fast, f) and (slow, s) in Figure 16a. Worth mentioning, the resulting broad NMR rate peak of the fast diffusing species resembles that obtained for microcrystalline Li_xSnS_2 before annealing. The low-T activation energy is, however, much lower and the

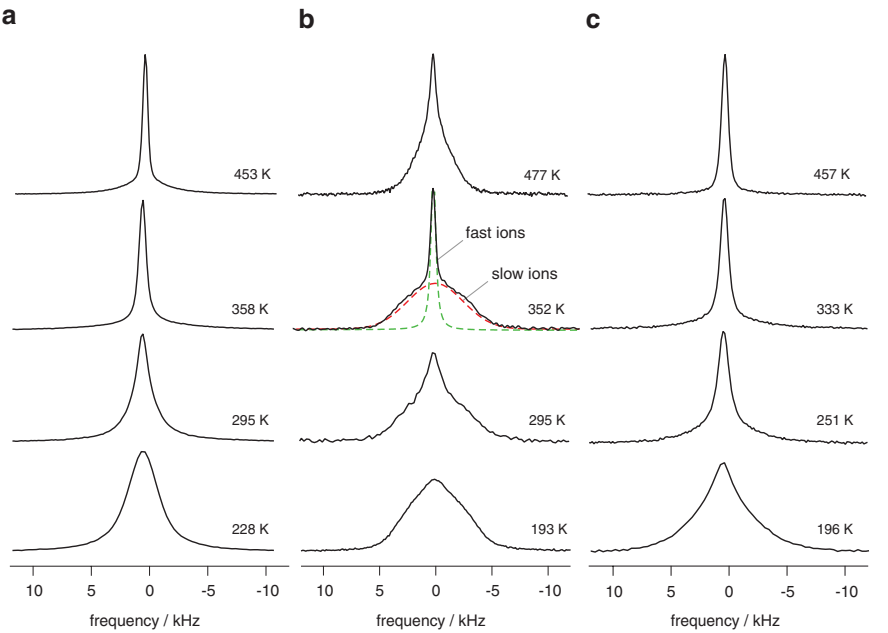

Fig. 17: ^{7}Li NMR line shapes (116 MHz) of (a) microcrystalline, i.e. coarse-grained $Li_{0.17}SnS_2$. (b) NMR spectra of a nanostructured sample with a mean crystallite size in the order of 10–20 nm. This sample contains a large volume fraction of amorphous material which is, in our opinion, represented by the broad, Gaussian-type NMR line (see the dashed lines that were used to deconvolute the overall signal recorded at 352 K). (c) Line shapes of a nanocrystalline sample that was synthesized via a mechanochemical route. Among the three samples it represents the fastest one in regard to Li ion self-diffusivity. This is also confirmed by ^{7}Li spin-lock SLR NMR relaxometry, see Figure 13a.

rate peak is shifted toward lower T as is illustrated by the horizontally drawn arrow in Figure 16a. This observation points to enhanced ion dynamics in the nanostructured form of Li_xSnS_2.

An additional increase in Li ion diffusivity is seen if we consider a sample that has been prepared via mechanochemical reaction of Li_2S and SnS_2 in a planetary mill, see the corresponding ^{7}Li NMR rates in Figure 16a. The shape of the Li NMR spectra do not reveal a pronounced structurally heterogeneous sample as discussed for the nanocrystalline sample before. We suppose that either defects introduced during the synthesize procedure are responsible for fast ionic diffusivity in the bulk or the surface-influenced regions. Heavy formation of amorphous regions, however, seems to slow down Li diffusivity at least in the case of layer-structured materials. Such materials already possess fast diffusion pathways being able to guide the ions also over long distances.

2.3 Enhancing ionic conductivity in poorly conducting ternary oxides and carbonates through structural disorder: $LiAlO_2$, Li_2TiO_3, $LiTaO_3$, $Li_4Ti_5O_{12}$, and Li_2CO_3

Lithium aliuminate is, at least in its γ-modification, known as a very poor ionic conductor if at hand in a coarse-grained or single-crystalline form. The Li ions occupy tetrahedral voids that are connected by corner-sharing. Recently, Wiedemann et al. compared experimental results on Li ion translational dynamics in oriented $LiAlO_2$ single crystals [orientations (100) and (001)] from (i) conductivity spectroscopy, (ii) mass tracer experiments as well as (iii) ^{7}Li NMR measurements. Ion transport turned out to be fully ionic [86]. For short-range Li ion dynamics ^{7}Li NMR relaxation resulted in an activation energy of ca. 0.7 eV, see Ref. [86] for an overview and Ref. [87] for recent measurements on a powder sample. The value of 0.7 eV agrees with that derived from neutron diffraction data that indicated a curved pathway connecting two adjacent Li sites in $LiAlO_2$ [88].

Long-range Li ion transport, on the other hand, has to be described with a higher activation energy [86, 89]. Both secondary ion mass spectrometry (SIMS) and conductivity spectroscopy revealed essentially the same activation energies of ca. 1.20(5) eV and 1.12(1) eV, respectively [86]. From 650 K to 750 K, which was the T range covered by the SIMS experiments, the diffusion coefficient D_{SIMS} equals D_σ meaning that the corresponding Haven ratio is given by $H_R = 1$ [86]. Note that in Ref. [86] the solid-state diffusion coefficient D_σ was estimated via the Nernst–Einstein equation by assuming that the number density of charge carriers is simply given by the lithium concentration of the oxide. Mechanical loss spectroscopy confirmed these diffusion coefficients and activation energies [89]. Dynamic mechanical analysis, which is sensitive to ultraslow Li ion displacements, points to a Debye-like motional correlation that controls ion dynamics at low temperatures. Recently, activation energies of ca. 1.1 eV have also been found via sin–sin correlation functions probed with the help of ^{7}Li stimulated echo NMR being sensitive to long-range transport, see Ref. [90].

Regarding microcrystalline powder samples a very similar activation energy of ca. 1.14 eV [47] is obtained from conductivity measurements for temperatures below 600 K (see Figure 18a), see also Ref. [86] for an overview. The low conductivities and diffusivities are highly welcome if $LiAlO_2$ is used as, e.g. blanket material in fusion reactors. In such systems diffusion should be strictly prevented. The application of the oxide in electrochemical storage systems, however, requires much better ion diffusivities. For instance, $LiAlO_2$ is considered to act as thin-film electrolyte in all-solid-state batteries prepared with the use of sputtering or other deposition techniques. Furthermore, it has been reported that the oxide can be used as coating for Li_x(Ni, Co, Mn)O_2-based cathodes [91]; Goodenough and

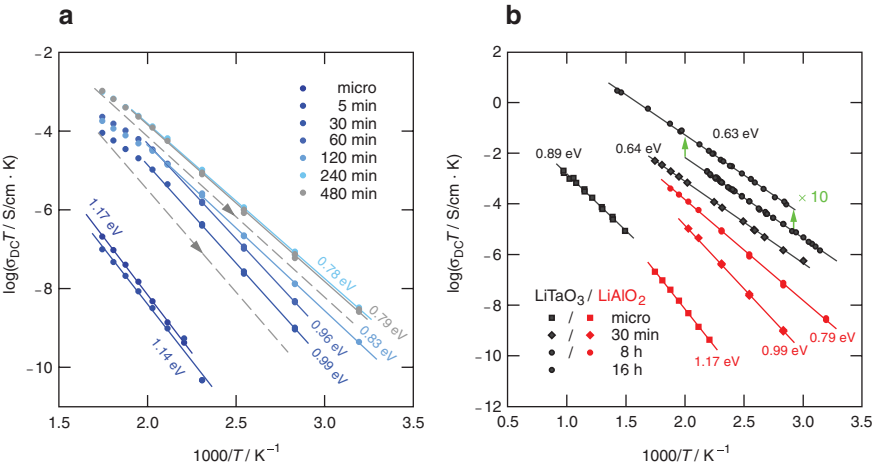

Fig. 18: (a) Ionic conductivities of micro- and nanocrystalline $LiAlO_2$. The latter was obtained by high-energy ball milling the starting material for the milling times indicated. For example, at 450 K the jump in conductivity is five orders of magnitude when going from the microcrystalline material to $LiAlO_2$ that was treated for 480 min in a planetary mill (Fritsch Pulverisette P7). (b) Comparison of the results obtained for nanocrystalline $LiAlO_2$ with those of high-energy ball milled $LiTaO_3$ that was prepared in a shaker mill. Note the data for the 8 h and the 16 h ball milled sample coincide. For better clarity, those of the 16-h-sample were shifted by a factor of 10 upwards. Figures adapted from Ref. [47].

co-workers [92] as well as Cheng et al. [93] have recently shown that during the preparation of the highly-conducting electrolyte $Li_7La_3Zr_2O_{12}$ (LLZO), doped with Al, the LLZO crystallites are often covered by an amorphous layer of $LiAlO_2$. Such a grain-boundary phase can have a negative impact on long-range ion transport in such oxide electrolytes.

Thus, also from an application point of view it seems to be important to study Li ion diffusion parameters in structurally disordered $LiAlO_2$. As is shown in Figure 18a high-energy ball milling significantly influences the DC conductivity of $LiAlO_2$ which can be read off from the frequency independent plateaus of the underlying conductivity isotherms. While overall conductivity has increased by several orders of magnitude, the activation energy decreases from 1.14 eV down to 0.78 eV (Figure 18a), [47]. The same effect is known for nanocrystalline $LiTaO_3$ (see Figure 18b), which has been studied in detail via conductivity spectroscopy and ^{7}Li NMR relaxometry in an earlier work [5].

In order to study the origins that cause the increase in conductivity, XRD, HR TEM and ^{27}Al magic angle spinning (MAS) NMR were employed [47], see also Figures 19 and 20a. In the case of $LiAlO_2$ powder XRD proves nanostructuring of

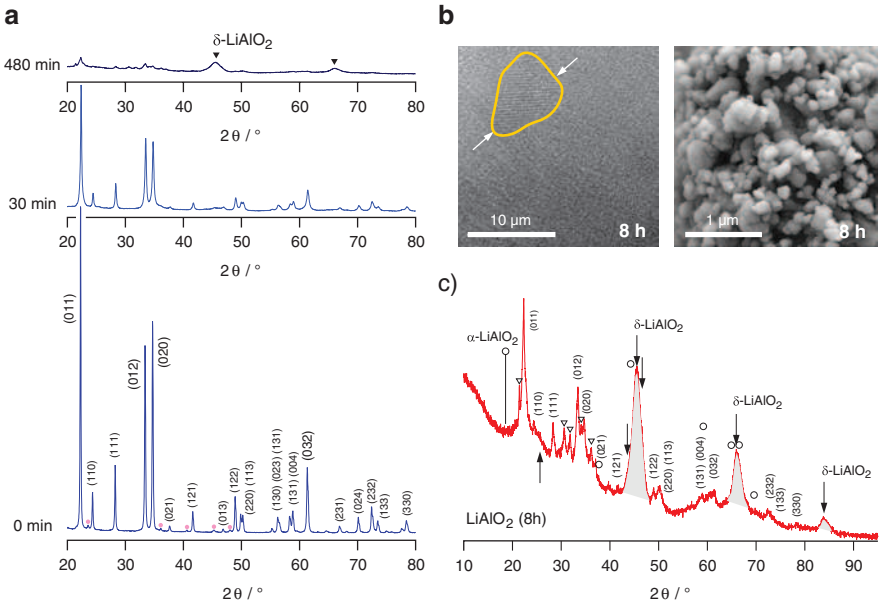

Fig. 19: (a) XRD powder patterns of micro- and nanocrystalline $LiAlO_2$. After 30 min of milling broadening of the reflections is seen but no other phases than the g-form show up. This changes when the milling time is raised to 8 h; the broad intensities at 45° and 67° point to δ-$LiAlO_2$ generated. Simultaneously, significant amounts of amorphous material are formed. (b) HR-TEM image and scanning electron microscopy picture of $LiAlO_2$ (milled for 8 h). (c) Magnification of the XRD pattern shown in (a). As is indicated by XRD, the formation of α-$LiAlO_2$ seems to be negligible. Figures adapted from Ref. [47].

the samples. While after 30 min a nanocrystalline ceramic of γ-$LiAlO_2$ has been obtained, further milling leads to the formation of large amounts of amorphous material and structurally disordered δ-$LiAlO_2$. The δ-form is a high-pressure modification of $LiAlO_2$. This observation was confirmed by ^{27}Al MAS NMR [47]. The more δ-$LiAlO_2$ is formed, the more intense the respective NMR signal at 15 ppm [referenced against $Al(NO_3)$ aqueous solution], which represents those Li ions residing on octahedral sites in the δ-modification. After 8 h of milling, $LiAlO_2$ nanocrystallites are obtained that are embedded in an amorphous matrix of the aluminate (see the HR TEM image shown in Figure 19b). The higher diffusivity in $LiAlO_2$ was also seen in ^7Li NMR line shape measurements [47], see Figure 20b.

Compared to $LiAlO_2$ the enhancement effect observed for $LiTaO_3$ is somewhat stronger. As one might expect because of the similar structure parameters, the behaviour of $LiTaO_3$ resembles that of nanocrystalline $LiNbO_3$. For Li_2TiO_3, on the other hand, the total increase in conductivity is less pronounced. The

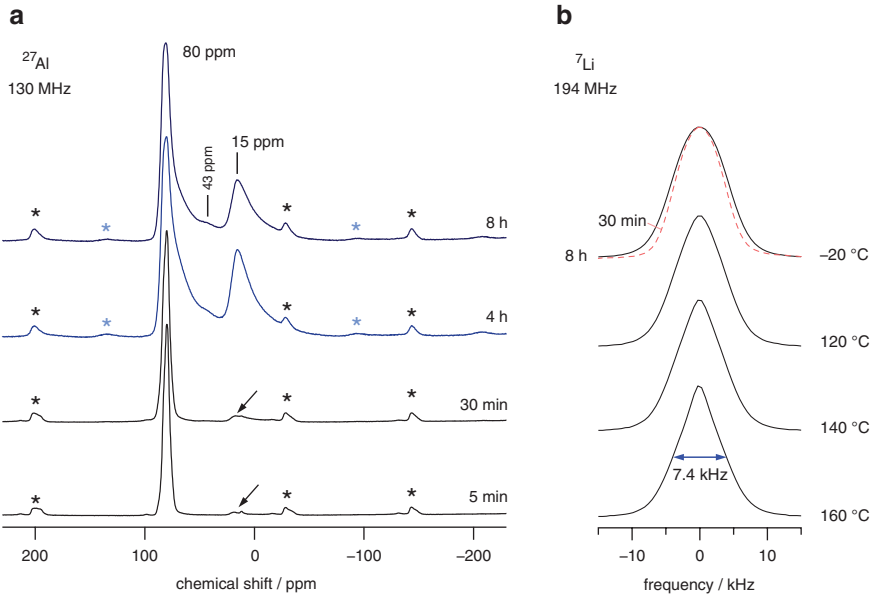

Fig. 20: (a) ^{27}Al MAS spectra of $LiAlO_2$ treated for the milling times indicated; chemical shifts refer to $Al(NO_3)$ 1 M aqueous solution. (b) ^{7}Li NMR line shapes at various temperatures for the sample milled for 8 h (and 30 min, for comparison). Above 140 °C the line shows noticeable narrowing due to Li jump processes with rates of the order of the rigid-lattice line width (see the line recorded at –20 °C). Spectra taken and adapted from Ref. [47].

latter is simply because the conductivity of microcrystalline Li_2TiO_3 is already higher than that of $LiTaO_3$ and $LiAlO_2$. The dashed lines in Figure 21a indicate the conductivities of $LiAlO_2$ and $LiTaO_3$ which were each milled for 8 h in the same planetary mill under the same conditions regarding the vial set and ball-to-powder ratio.

Quite recently, we studied the change in local structure of Li_2TiO_3 and $LiTaO_3$ through (extended) X-ray absorption fine structure (EXAFS) measurements similar to earlier work on $LiNbO_3$ [4]. As an example, in Figure 21b EXAFS data and Fourier transforms are presented for un-milled and mechanically treated Li_2TiO_3. The XAS scans were collected for the appropriate edge (Ti K-edge and Ta L3-edge) at room temperature on beam line B18 at the Diamond Light Source (Oxfordshire). For Li_2TiO_3, ball-milling attenuates the EXAFS and we observed a decrease in the height of the Ti–Ti peak in the Fourier transform. Similar results were also obtained for ball-milled $LiTaO_3$ [5] that was treated in a planetary mill (Figure 22). In Figure 23a and b the conductivities of several samples as well as the corresponding isotherms of a sample milled for 30 min are shown.

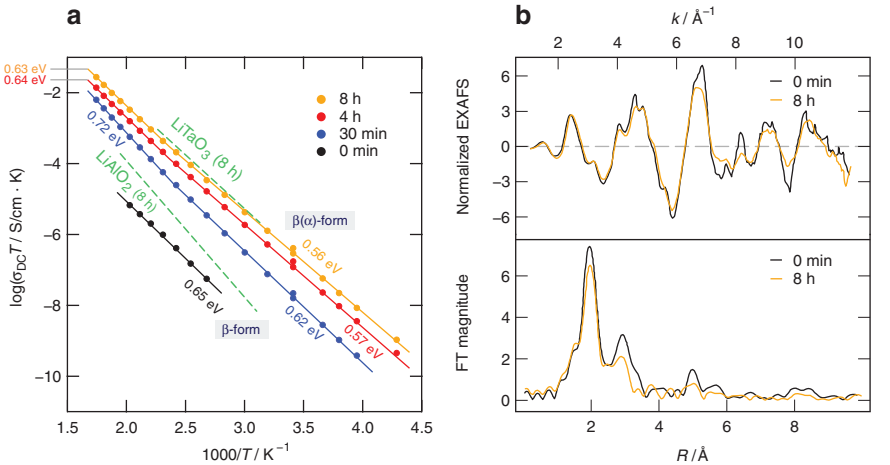

Fig. 21: (a) Arrhenius plot showing the temperature dependence of $\sigma_{DC}T$ of micro- and nanocrystalline β-Li_2TiO_3. Note that, according to X-ray diffraction, after 8 h of milling a mixture of amorphous Li_2TiO_3, the β-form and the α-modification has been formed. The dashed lines indicate conductivities of $LiTaO_3$ and $LiAlO_2$ each milled for 8 h, for comparison. (b) Normalized EXAFS data of the source material and the sample milled for 8 h in a planetary mill; (b) Fourier transforms (FT) of the k^3 weighted normalized EXAFS data shown at the top. The data were analyzed to yield details on the local structure, i.e. bond lengths, *R*, Debye–Waller factors, σ_{DW}. Figures taken from Refs. [27, 48] .

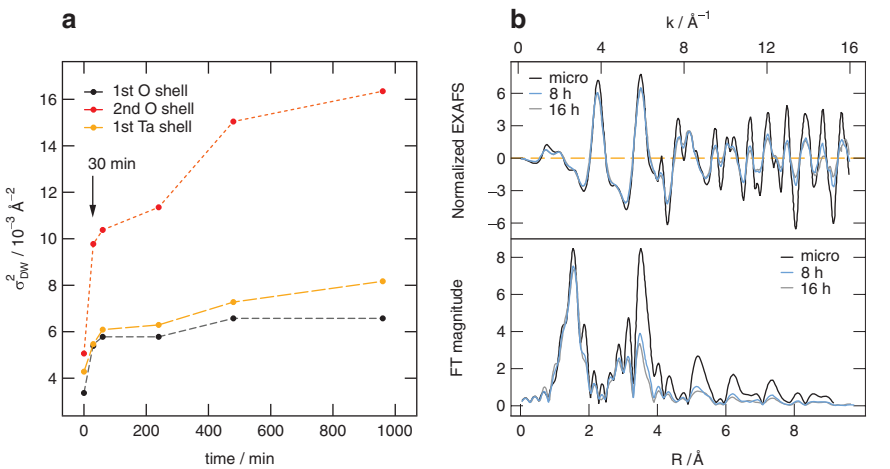

Fig. 22: (a) Change of the Ta L_3-edge EXAFS Debye–Waller factors, plotted as σ^2_{DW}, of nanocrystalline $LiTaO_3$. (b) The Ta L_3-edge EXAFS of $LiTaO_3$, the upper graph shows normalized spectra, the lower one the corresponding Fourier transforms. See Ref. [48] for further details.

For $LiTaO_3$ the decrease in EXAFS is best seen for the Ta–O and Ta–Ta correlations at ca. 2.0 Å and 3.8 Å, respectively (Figure 22b). The effect was analyzed in two ways *viz*. as a change in the Debye–Waller factor σ_{DW} due to (microscopic) disorder and as the effect of amorphous regions introduced during milling. Considering the Debye–Waller factors, shown in the form of σ^2_{DW} vs. milling time, for all the correlations σ^2_{DW} almost doubles after the oxide has been treated for only 30 min (Figure 22a). It can be explained that already after short periods of milling the local structure around the Ta ions is somewhat distorted. With increasing milling the Ta–O Debye–Waller factors show only a gradual change whereas the Ta–Ta correlation, which is significantly larger, continues to increase steeply with increasing mechanical treatment. We assume that at the beginning of the milling process the local Ta–O octahedra are affected while the relative arrangement of the octahedra continues to change with further treatment. Such observation would be expected given that the strong Coulomb interaction between Ta^{5+} and O^{2-} will maintain a relatively rigid local structure.

In an earlier study we used a shaker mill (SPEX 8000) equipped with a single ZrO_2 ball (10 mm in diameter) and a zirconia vial to produce nanocrystalline $LiTaO_3$. After 30 min of milling most of the local electric field gradients in the direct neighborhood of the Li nuclei are still comparable to those in un-milled, coarse-grained $LiTaO_3$. Many hours of milling were needed to destroy the originally well-structured powder pattern. Interestingly, the largest increase in ion conductivity is seen when the sample is milled for 30 min. Obviously, considering ion dynamics in $LiTaO_3$, (local) distortions, point defects, displacements and strain introduced during the first 30 min of milling is sufficient to have a remarkable effect on both short-range as well as long-range ion transport. Interestingly, the previous conductivity studies [5] revealed some subtle dependence of the microstructure on the time of ball-milling. The longer the milling time the more difficult it is to recover crystallinity by thermal annealing. Hence, the additional conductivity enhancement seen for longer milling times is presumably due to the increasing formation of amorphous fractions.

In the case of planetary mills the situation is similar but also entails some differences. For planetary mills, enabling heavy grinding, indeed the generation of amorphous materials is more likely. Although for both types of mills amorphous material is expected to be formed at longer milling times, planetary mills might already produce significant amounts of amorphous material at short milling times. In Figure 23a and b the conductivity results of such samples are shown; they were prepared in planetary mills equipped with up to 140 small milling balls with a diameter of 5 mm only. As can be clearly seen from the Arrhenius plots the ionic conductivity reached an upper limit already after 30 min. Considering the corresponding complex plane plots and capacities of the data, the DC plateaus

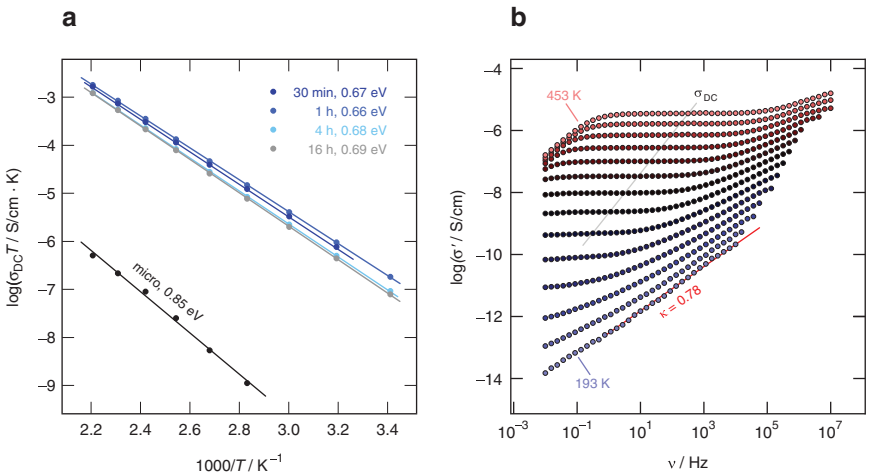

Fig. 23: (a) Temperature dependence of the ionic conductivity of $LiTaO_3$ if treated in a planetary mill for the times indicated. The values for unmilled $LiTaO_3$ are also shown. (b) Conductivity isotherms of $LiTaO_3$ high-energy ball milled for 30 min in a planetary mill. κ denotes the exponent in $\sigma' \propto \nu^{\kappa}$ used to approximate the behaviour in the dispersive regions.

in Figure 23b have to be characterized by capacities typically found for bulk responses that are already affected by the influence of the electrical response of grain boundaries (see Figure 24a).

Milling $LiTaO_3$ for 30 min causes the activation energy to decrease from 0.85 eV to 0.67 eV. Simultaneously, the corresponding pre-factor of the Arrhenius relation increased by 1.5 orders of magnitude. Such an increase might be attributed to free volume generated and structural disorder generated. Longer milling times do not influence the Li ion conductivity further. Once again, after 30 min the extent of structural disorder, i.e. local defects and amorphous material, has already reached a critical level to generate a network of fast migration pathways. We expect the percolating amorphous regions to form such a network. This view is supported by the abrupt change of the corresponding ^{7}Li NMR line shapes observed (Figure 24b). Already after 30 min of milling the ^{7}Li NMR spectrum resembles that of a sample milled for 8 h rather than that of the source material. The samples produced in planetary mills can thus be regarded as heterogeneously disordered materials, i.e. they are composed of (defect-rich) crystalline grains being embedded in an amorphous matrix that ensures fast long-range ion transport.

According to this explanation we alternatively assumed that the attenuation seen in EXAFS of the samples prepared with planetary mills (Figure 22b) stems

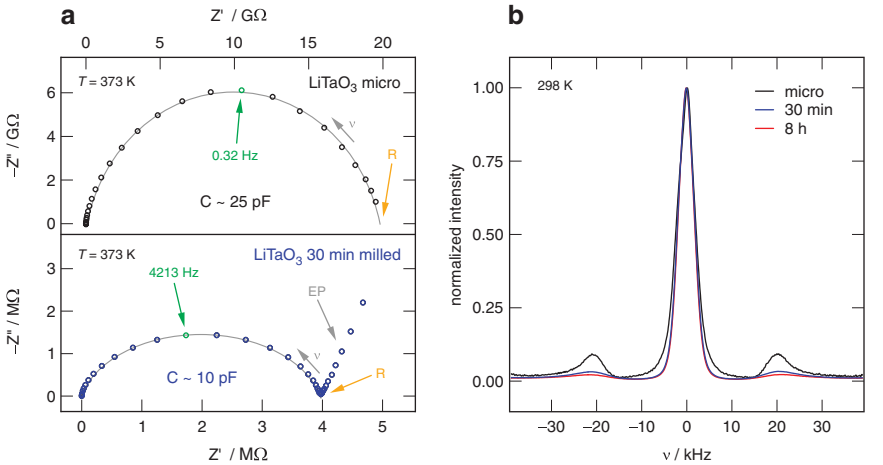

Fig. 24: (a) Nyquist plots of the complex impedance (373 K) of microcrystalline $LiTaO_3$ (upper graph) and nanocrystalline $LiTaO_3$ (milled for 30 min). Note that the two graphs refer to two axes with quite different scale markings which illustrates once more the giant increase in conductivity observed. (b) ^7Li NMR spectra of microcrystalline $LiTaO_3$ and two samples milled for 30 min and 8 h, respectively. Since ^7Li is a spin-3/2 nucleus, the spectrum is composed of a central line flanked by satellite intensities as the nuclear quadrupole moment interacts with electric field gradients in its direct neighborhood. This interaction alters the Zeeman levels in such a way that, according to the orientation of the crystallites with respect to the magnetic field, satellite intensities arise. In the present case, single pulse spectra are shown and the resulting quadrupole powder pattern is, of course, less developed than in the case of echo spectra. Nevertheless, this way the decrease in intensity of the 90° singularities is best seen. For the milled samples only a shallow difference is detected that is in line with the results from conductivity spectroscopy and EXAFS.

only from the amorphous material generated. If we take the Ta–Ta correlation as an indirect (relative) measure for the amount of amorphous $LiTaO_3$ produced, milling for as little as 30 min is estimated to yield already ca. 25 % amorphous material. This parallels the ionic conductivity measurements of the same sample ball-milled for 30 min where the magnitude is four orders higher than that for an un-milled sample (see the data at 360 K). After 8 h of milling, EXAFS suggest that the amount of amorphous $LiTaO_3$ has increased to approximately 60 %. This additional increase has, however, no further effect on the ionic conductivity presented in Figure 23a.

A similar steep increase in conductivity has recently been found for Li_2CO_3, see Figure 25. Lithium carbonate is an important constituent in the passivating interlayer, the so-called solid electrolyte interface (SEI), in liquid-based secondary lithium-ion batteries. During charging and discharging the battery the Li ions

have to surmount this barrier of decomposition products. Thus, the ionic conductivity of its components is key to guarantee powerful cycling and rate capability, particularly if an SEI mainly composed of by Li_2CO_3 is considered. To mimic the presumably amorphous Li_2CO_3 formed inside a battery, we treated microcrystalline Li_2CO_3 to introduce defect structures and to push its conductivity to the upper reachable limit of ion dynamics. As has been seen for $LiAlO_2$, Li_2TiO_3 and $LiTaO_3$, σ_{DC} already increases by several orders of magnitude if treated for short times in planetary mills. The same effect is seen for the carbonate, Figure 25a. The increase in conductivity is accompanied by a decrease of the original activation energy (1 eV) of coarse-grained polycrystalline Li_2CO_3; after 2 h of milling it decreased to 0.66 eV. This value as well as the conductivities obtained almost coincide with those for $LiTaO_3$ that served as an internal benchmark, see the dashed line in Figure 25a.

As compared to the oxides discussed so far, for the titanate $Li_5Ti_4O_{12}$, which is a well-known zero-strain anode material for lithium-ion batteries, the effect of ball milling on Li^+ dynamics is much lower. Although ionic conductivity in microcrystalline $Li_4Ti_5O_{12}$ is poor [94], viz. in the order of 10^{-12} S cm^{-1} at 295 K (ca. 0.76 eV, depending on the defect chemistry and exact morphology [27, 95]), it is, however, by about 1 order of magnitude higher than that of Li_2TiO_3. Milling of $Li_4Ti_5O_{12}$ for

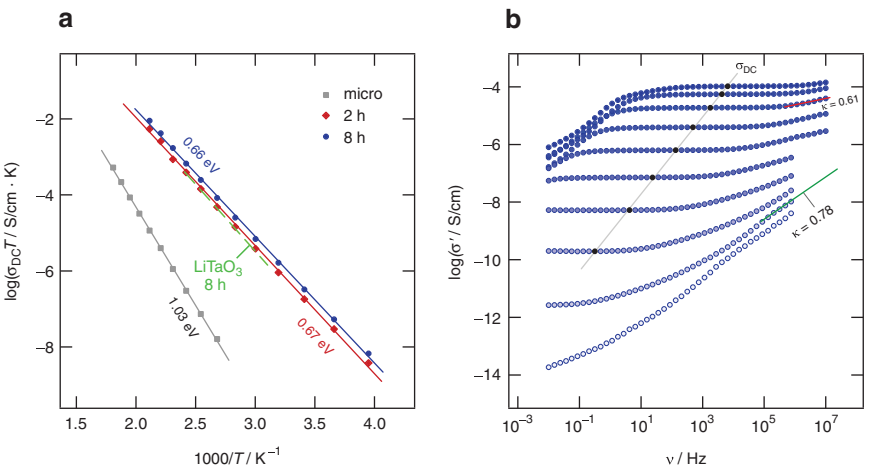

Fig. 25: (a) Change of $\sigma_{DC}T$ of un-milled and milled Li_2CO_3 as a function of the inverse temperature. At 370 K, an increase of σ_{DC} by four orders of magnitude is seen; E_a decreases from ca. 1 eV to 0.66 eV (8 h milling). As a benchmark also the Arrhenius line of nanocrystalline $LiTaO_3$ (8 h, planetary mill) is shown. (b) The corresponding conductivity spectra from which the values σ_{DC} were read off. κ denotes the exponent in $\sigma' \propto \nu^{\kappa}$ used to approximate the behaviour in the dispersive regions.

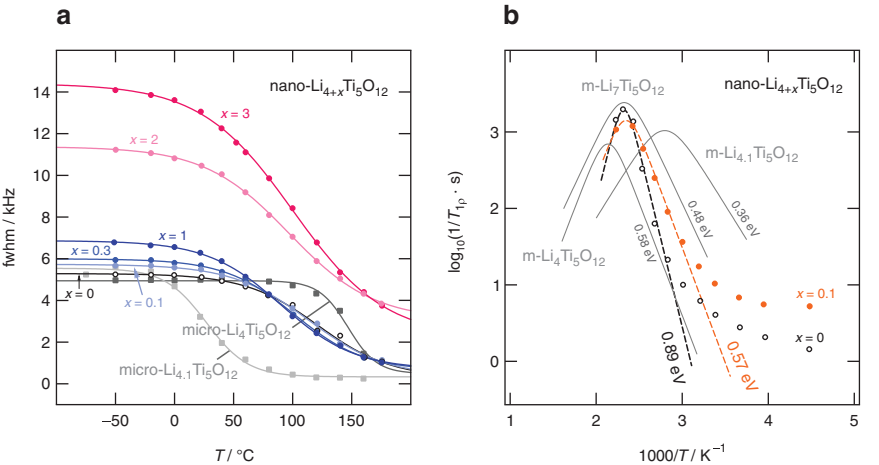

Fig. 26: (a) Li diffusivity in nanocrystalline $Li_{4+x}Ti_5O_{12}$ ($x = 0$, 0.1, 0.3, 1, 2, 3) as seen via ^{7}Li NMR line widths measurements and (b) spin-lock relaxometry carried out a locking frequency of 30 kHz; the samples with $x = 0$ and $x = 0.1$ are shown. Compared to microcrystalline $Li_4Ti_5O_{12}$ the Li diffusivity in the nanocrystalline form ($x = 0$) is slightly enhanced. If nano-$Li_4Ti_5O_{12}$ is, however, treated with *n*-BuLi to form nano-$Li_{4.1}Ti_5O_{12}$ no significant change in Li ion mobility is seen via NMR. This is quite different for the microcrystalline form, for which we observed a steep increase in Li diffusivity when going from $Li_4Ti_5O_{12}$ to $Li_{4.1}Ti_5O_{12}$, see (b). The diffusion-induced relaxation rate peak of microcrystalline $Li_7Ti_5O_{12}$ is shown for comparison.

4 h in a planetary mill causes σ_{DC} to increase by only 0.5 orders of magnitude (330 K). The activation energy is reduced from 0.76 eV to 0.69 eV.

This relatively small effect can also be observed via ^{7}Li NMR relaxometry and complementary line widths measurements. The results shown in Figure 26 refer to nanocrystalline $Li_4Ti_5O_{12}$, which was prepared by high-energy ball milling in ethanol for 3 h. The open symbols in Figure 26a represent the ^{7}Li NMR motional narrowing curve of nanocrystalline $Li_4Ti_5O_{12}$. The curve resembles that of microcrystalline $Li_4Ti_5O_{12}$, which is shown for comparison. The onset of motional narrowing for nano-$Li_4Ti_5O_{12}$ is, however, shifted by 50 K toward lower temperatures revealing (slightly) enhanced ion diffusivity. Most interestingly, if Li is chemically inserted into nanocrystalline $Li_4Ti_5O_{12}$ no drastic change of the motional narrowing (MN) curve is seen if x values of up to 0.3 are considered, Figure 26a. For micro-$Li_4Ti_5O_{12}$ the same treatment in *n*-BuLi causes a significant enhancement of ion mobility – the corresponding MN curve is shifted by almost 150 K toward lower T [96]. The situation for x being larger than 0.3 is more difficult to explain as the increased Li^+–Ti^{3+} interactions additionally broaden the spectra. A significant dependence of Li ion diffusivity on x, as it has been documented for the unmilled form [96, 97], seems to be, however, absent.

The same characteristic for nanocrystalline $Li_4Ti_5O_{12}$ and nano-$Li_{4.1}Ti_5O_{12}$ is seen if we look at the ^{7}Li NMR spin-lock relaxation rates presented in Figure 26b. The corresponding diffusion-induced relaxation rate peaks for $x = 0$ and $x = 0.1$ show up at essentially the same temperature. By coincidence it is what we also found for microcrystalline $Li_7Ti_5O_{12}$. In contrast, the difference for microcrystalline $Li_4Ti_5O_{12}$ and micro-$Li_{4.1}Ti_5O_{12}$ is much larger. Hence, we conclude that in the case of $Li_4Ti_5O_{12}$ the introduction of structural disorder is much less favorable for ionic diffusivity. By comparing the results for micro- and nanocrystalline $Li_4Ti_5O_{12}$ from rotating-frame spin-lock NMR an interesting feature is revealed: although the rate peak of the nanocrystalline sample shifts to lower T, as is expected when comparing the respective MN curves, the low-T flank of nano-$Li_4Ti_5O_{12}$ has to be characterized by a higher activation energy. This feature can only be explained by an enhanced pre-factor of the associated Arrhenius law. If x is increased from $x = 0$ to $x = 0.1$ we witness both a decrease of E_a (from 0.89 eV to 0.57 eV, see Figure 26b) and the associated pre-factor. Without any change of the pre-factor the position of the rate peak should have been changed to be in agreement with a higher mean activation energy.

2.4 Ionic conductivity in nanocrystalline Li_2O_2 and Na_2O_2 – the possible discharge products in Li- and Na-air batteries

Ionic conductivity and diffusivity in peroxides belongs to the white areas of materials science. Li_2O_2 and Na_2O_2 form during discharging a Li metal or Na metal oxygen battery. Elucidating the transport properties of the ionic and electronic charge carriers in these peroxides is of importance in the field of oxygen batteries. Considering the above derived conclusion that ion transport can be, in some cases, greatly enhanced if the poorly conducting oxides were mechanically treated, we tried the same approach to produce phase-pure nanocrystalline Li_2O_2 and Na_2O_2. Thus, we expect that with nanocrystalline, ball-milled Li_2O_2 a material with an upper limit of reachable ion conductivities is at hand. To determine these maximal conductivity parameters might also influence current battery research on metal oxygen systems.

Li_2O_2 crystallizes with the hexagonal space group $P6_3/mmc$ and shows two crystallographically distinct Li sites (Wyckoff positions 2a and 2c). The covalently bonded O_2 dimers are arranged in an alternating ABAB stacking. The trigonal prismatic Li ions in Li_2O_2 are in the same layer as the peroxide anions. The octahedrally coordinated ones reside between the peroxide layers. As revealed by impedance and conductivity spectroscopy Li ion transport in Li_2O_2 is extremely low [29, 98]. In Figure 27a the corresponding overall conductivities of microcrystalline

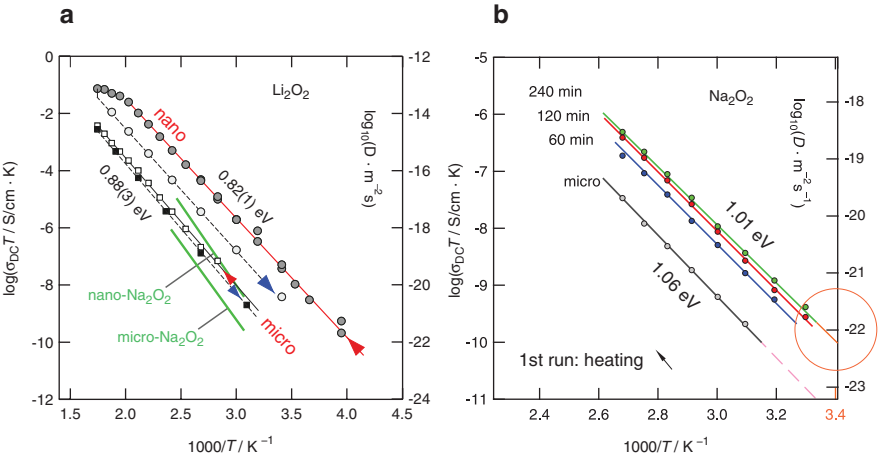

Fig. 27: (a) Arrhenius diagram of the overall conductivities of microcrystalline and nanocrystalline Li_2O_2. The arrows indicate the heating and cooling runs. At high temperatures nanocrystalline Li_2O_2 is exposed to grain growth and healing of defects, thus a decrease in conductivity was seen during cooling. For microcrystalline Li_2O_2 almost no difference was detected. For comparison, the Arrhenius lines of micro- and nanocrystalline Na_2O_2 are also shown. (b) Total Conductivity of micro- and nanocrystalline Na_2O_2 obtained after high-energy ball milling the coarse-grained starting material. The right axes refer to solid-state diffusion coefficients which were obtained by means of the Nernst–Einstein equation using the σ values measured. Figures adapted from Refs. [29, 46].

and nanocrystalline Li_2O_2 are compared with those of isostructural Na_2O_2 [46], see also Figure 27b. While high energy ball milling of Li_2O_2 causes the total conductivity to increase by approximately 2 orders of magnitude, in the case of Na_2O_2 the effect is much less pronounced. For micro-Li_2O_2 we obtained a very low conductivity of 3.4×10^{-13} S/cm at ambient temperature [29]. High-energy ball-milling leads to an increase of σ_{DC} by ca. 2 orders of magnitude reaching 1.1×10^{-10} S/cm; correspondingly, the activation energy decreases from 0.89 eV to 0.82 eV. The electronic contribution to σ, which was measured via polarization experiments, turned out to be in the order of 9×10^{-12} S/cm. This values makes <10 % of the total conductivity. For ball-milled Na_2O_2 at ambient conditions the overall conductivity is in the order of 10^{-13} S/cm. Recent polarization experiments have shown that the partial electronic conductivity ranges between 7.6×10^{-14} S/cm and 1×10^{-13} S/cm. Thus, the total conductivity in the sodium analogue is to a non-negligible extent influenced by electronic charge transport.

The poor ionic conductivity of Li_2O_2 is also represented by ^{7}Li NMR line shape measurements [29]. Interestingly, the ^{7}Li NMR lines of nano-Li_2O_2 undergo a pronounced heterogeneous motional narrowing upon heating the peroxide,

see Figure 28a. The Gaussian shaped NMR line that is seen in the regime of the rigid lattice narrows such that a two-component line shape emerges. The narrow line on top of the broader one represents Li ions being mobile on the time scale defined by the line width at low T, i.e. these ions have access to diffusion processes being characterized by (mean) jump rates in the order of ca. 20 kHz. Most likely, the enhancement in conductivity can be traced back to the generation of a small spin reservoir with mobile Li ions; these are expected to reside in the direct neighborhood of defects generated or near the structurally disordered and defect-rich interfacial regions formed during mechanical treatment.

Through ^{7}Li NMR relaxometry and stimulated echo measurements we could refine the picture presented by conductivity spectroscopy. Interestingly, the diffusion-induced NMR relaxation rates reveal much lower activation energies for Li ion dynamics in Li_2O_2 (0.22–0.24 eV, see Figure 28b). Obviously, the rates probe local or short-range motions rather than long-range ion transport. We may

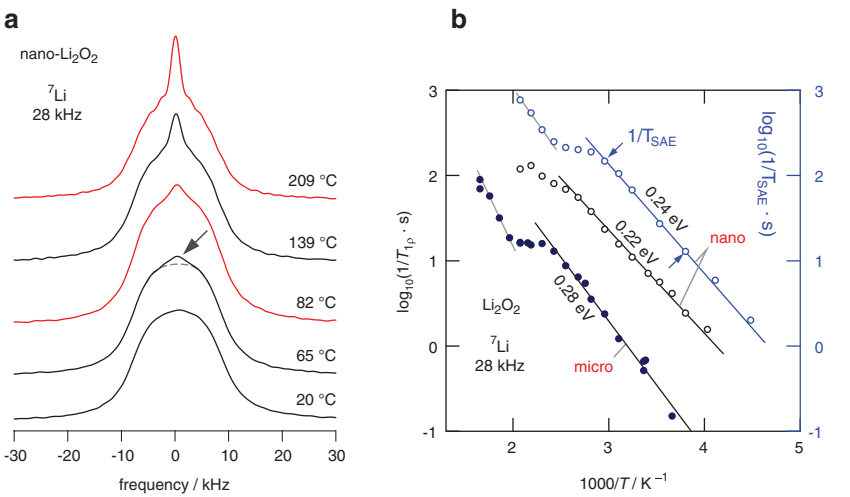

Fig. 28: (a) ^{7}Li NMR line shapes of nanocrystalline Li_2O_2 that was mechanically treated for 3 h in a planetary mill equipped with a milling vial made of ZrO_2. With increasing T a two-component NMR line shape emerges; the narrow line superimposing the broad one reflects relatively mobile ions in nanocrystalline Li_2O_2. (b) ^{7}Li NMR spin–lattice relaxation rates of nanocrystalline Li_2O_2 recorded in the laboratory frame (116 MHz) and in the rotating frame of reference (28 kHz locking frequency). At temperatures lower than ca. 370 K the rates reveal Arrhenius behaviour with a much lower activation energy than detected by conductivity spectroscopy. The same temperature dependence is seen via ^{7}Li SAE NMR if temperatures lower than 330 K are considered (0.24 eV). The discrepancy in E_a clearly points to heterogeneous dynamics with subsets of slow and fast Li ions. The latter predominantly govern the overall NMR rates in this T regime. Figures adapted from Ref. [29].

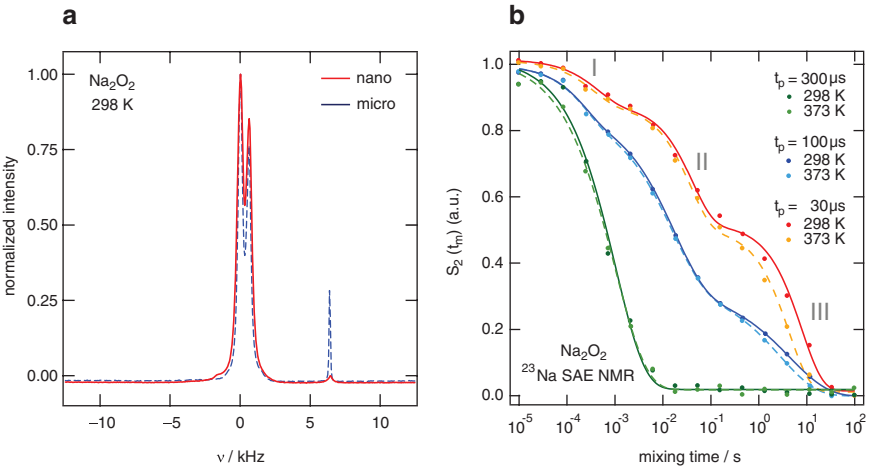

Fig. 29: (a) ^{23}Na MAS spectra of micro- and nanocrystalline Na_2O_2. The spectra were recorded at 132.25 MHz and a spinning speed of 30 kHz. Apart from the two main signals, another line (Na_2O) shows up at higher frequencies. (b) ^{23}Na SAE NMR decay curves of microcrystalline Na_2O_2 recorded at the preparation times and temperatures indicated.

identify the fast subset of Li ions seen in line shape NMR to be responsible for the low E_a values deduced through relaxometry. The same seems to be the case for the ^{7}Li SAE NMR decay rates that are shown in Figure 28b for comparison. At higher T we recognized another thermally activated process that is, in the case of T_1 ^{7}Li NMR relaxation, governed by a higher activation energy of 0.47 eV. A similar increase in decay rates is also seen in SAE NMR (0.41 eV). Most likely, this process is influenced by polaron dynamics; such dynamics were, for example, studied by first-principle calculations by Radin and Siegel who calculated an activation energy of 0.42 eV [99].

In analogy to Li_2O_2 we started to analyze the poor Na ion diffusion in nano- and microcrystalline Na_2O_2, see Figure 27a. High-resolution (MAS) ^{23}Na NMR measurements carried out at 132.25 MHz revealed the two magnetically inequivalent Na sites in Na_2O_2 as expected, see Figure 29a. The spectra shown were recorded at a spinning speed of 30 kHz, no reference was used to measure the chemical shift values; the more intense signal was simply referenced to 0 kHz. Krawietz et al. report chemical shifts of 4.8 and 9.9 ppm [100]. Slow Na ion hopping between the two neighbored sites might be measure bale via 2D exchange NMR or SAE NMR. Preliminary ^{23}Na SAE NMR decay curves of microcrystalline Na_2O_2 are shown in Figure 29b; to the best of our knowledge this is the first time that such curves are reported for ^{23}Na. So far, the SAE technique has been successfully applied to ^{2}H [101, 102], ^{9}Be [71, 103, 104] and the two Li isotopes (^{6}Li and ^{7}Li, [63, 69, 71, 72]).

Extending the technique to the ^{23}Na ($I = 3/2$) nucleus is, however, limited because of the large quadrupole moment of the Na spin that hinders a non-selective excitation. In the present case, the ^{23}Na SAE signal is a mixture of quadrupolar and dipolar contributions.

Although the ^{23}Na SAE S_2 curves recorded at fixed t_p and variable t_m sensitively depend on preparation time, they do not significantly vary with temperature. Hence, Na ion dynamics in microcrystalline Na_2O_2 is by far too poor to be detectable even with NMR methods designed to probe slow ion exchange. The curves recorded at short t_p are clearly composed of three decay steps. While step III reflects the almost T independent T_1 relaxation, step II is most likely driven by spin-diffusion effects. The first decay step seems to be associated with transversal spin–spin relaxation.

2.5 Glass formers: the influence on ball milling on ion transport in crystalline $Li_2B_4O_7$

As has been illustrated above for several oxides, particularly for $LiTaO_3$, $LiAlO_2$ and Li_2CO_3, mechanical treatment can greatly enhance Li ion diffusivity and Li ion transport, respectively. Expectedly the same is true for glass formers such as $Li_2B_4O_7$ that served as another model substance to quantify the effect of high-energy ball milling on DC conductivity [28], in a second step the transport parameters could directly be compared with those of the pure glass that was prepared by quenching a melt of $Li_2B_4O_7$. For coarse-grained polycrystalline $Li_2B_4O_7$ the conductivity isotherms revealed low DC-conductivities and a quite high activation energy of 1.05 eV (see Figure 30). Milling in planetary mills has once again a drastic effect on ion transport. Interestingly, after 8 h of mechanical treatment we reached ionic conductivities that coincide with those of $LiAlO_2$ also milled for 8 h. Increasing the milling time to 16 h results in an additional increase of σ_{DC} by 0.5 orders of magnitude. Comparing a 16-h ball-milled sample and glassy $Li_2B_4O_7$ shows that there is still a large conductivity gap between the two samples, see Figure 30a.

X-ray powder diffraction suggested that the formation of amorphous $Li_2B_4O_7$ is mainly responsible for the increase in ion dynamics. This view is supported by ^{11}B MAS NMR (Figure 31b), cf. Ref. [28]. Concerning ion dynamics, ^7Li NMR line shapes revealed that in addition to the ions in the amorphous regions also those in the crystalline grains nano-$Li_2B_4O_7$ do sense the effect of mechanical treatment; the motional narrowing curve depicted in Figure 30 b unveils the increase in ion dynamics seen in the wake of mechanical treatment. Presumably, defects introduced into the still crystalline grains also drastically influence local hopping

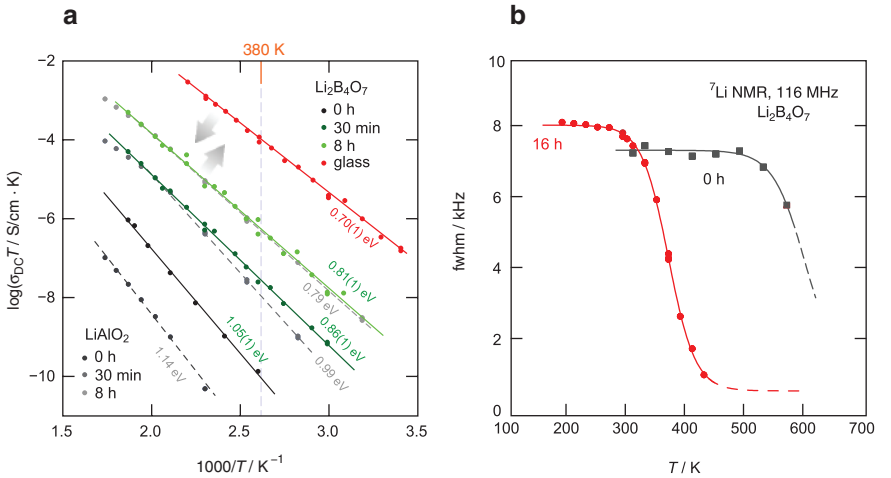

Fig. 30: (a) DC conductivities of nanocrystalline $Li_2B_4O_7$ produced through milling of the microcrystalline source material. For comparison, the results obtained for $LiAlO_2$ are also shown (see dashed lines). The solid lines represent Arrhenius fits, activation energies are indicated. The highest conductivities were obtained for a glassy sample ($E_a = 0.7$ eV). The arrows indicate the change in DC conductivity upon further mechanical treatment of the nanocrystalline material and the glass, respectively. (b) Change of the ^{7}Li NMR (central) line width of nano- and microcrystalline $Li_2B_4O_7$ with temperature. Figures adapted from Ref. [28].

processes. These local ion dynamics are characterized by only 0.3 eV as could be deduced from the low-T flank of the ^{7}Li SLR NMR rate peak (see Figure 31a). For comparison, the flank for micro-$Li_2B_4O_7$ is characterized by 0.5 eV.

$Li_2B_4O_7$ and aluminosilicates easily form glasses if the materials are melted and quenched. Although plenty of studies can be found in literature that deal with ion transport phenomena and diffusion mechanisms in glasses only few report on the change of ion transport parameters if glasses were mechanically treated in shaker or planetary mills. At first glance one would expect no significant influence when an already disordered material is milled. So far only few reports, however, showed that high-energy ball-milling of glassy materials ($LiAlSi_2O_6$ (β-spodumene, [105]), $LiBO_2$ [20, 106]) results in a decrease of the ionic DC conductivity, see also Ref. [107]. The same effect was observed for β-eucryptite [108]. This astonishing decrease was also confirmed by ^{7}Li NMR spectroscopy. For a first interpretation a simple structural model was used to explain the observed trend [105]. This effect is obviously caused by a mechanically induced structural relaxation of the non-equilibrium structure of the glass that was prepared by rapid thermal quenching [105]. Such structural relaxation obviously causes the ionic charge carriers to slow down with respect to those residing in the unmilled

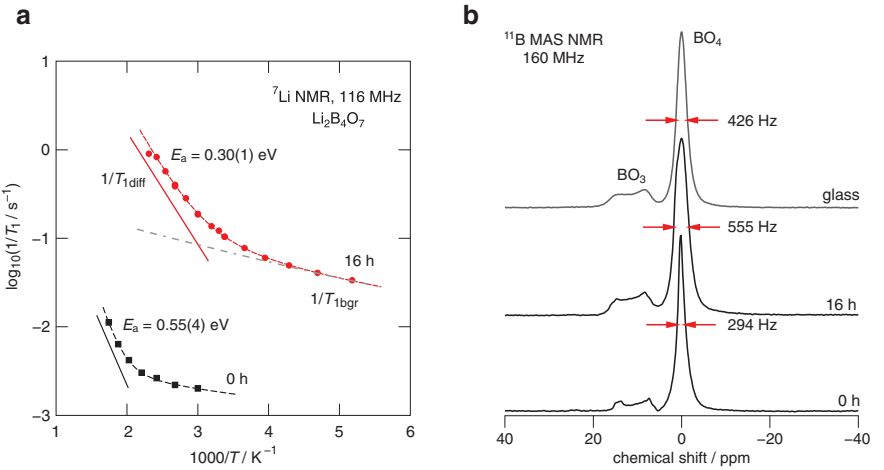

Fig. 31: (a) ^{7}Li NMR SLR rates of micro- and nanocrystalline lithium tetraborate $Li_2B_4O_7$. Unmilled $Li_2B_4O_7$ is characterized by extremely long longitudinal relaxation reaching 500 s at ambient temperature. After mechanical treatment the rate has increased to 5 s. Accordingly, the activation energy decreased from 0.55 eV to ca. 0.3 eV. Milling affected both the non-diffusive relaxation rates, the so-called background relaxation ($1/T_{1\,bgr}$), as well as the diffusion-induced contribution to the overall rate. Besides the introduction of (paramagnetic) impurities, $1/T_{1\,bgr}$ is also expected to be influenced by strictly localized (caged) ion dynamics. (b) ^{11}B MAS NMR spectra of micro- and nanocrystalline $Li_2B_4O_7$. The two resonances reflect the BO_4 and BO_3 units in $Li_2B_4O_7$. Milling causes the lines to broaden; this broadening can be assigned to polyhedra distortions because of mechanical treatment in the planetary mill. After 16 h of milling the line shape resembles that of amorphous $Li_2B_4O_7$. Figures adapted from Ref. [28].

glass matrix. Note that, influenced by the Löwenstein rule, for β-eucryptite, for example, stable and metastable forms with respect to the Al and Si ordering exist in certain temperature ranges. Ball-milling might largely influence local and long-range arrangements of the polyhedra. Hence, the structural arrangement in a quenched glass should not necessarily be identical with that of a milled sample.

3 Summary

Nanostructured materials are of large and ever growing interest due to their beneficial properties. In particular, nanocrystalline ceramics find applications as catalysts, sensors, adsorbents or new electrolytes and advanced electrode materials in electrochemical energy storage. We reviewed recent studies on lithium-ion dynamics and electrochemical activity of various classes of materials.

Nanostructuring is essential for TiO_2 to use the oxide as anode material in lithium-ion as well as sodium-ion batteries. We noticed marked differences in the storage mechanism when amorphous TiO_2 nanotubes are used as active material; the electrochemical reaction with sodium is significantly affected by interfacial effects. Li NMR spectroscopy measurements point to slow Li ion self-diffusivity in the amorphous form. Similarly, poor to moderate ion dynamics also govern ion transport in the other forms of titania such as rutile nanorods or mesoporous TiO_2. In the case of TiO_2-B nanotubes a fast relaxing reservoir of spins is detected that might be ascribed to those ions being located in the surface-influenced regions.

The formation of nanocrystalline ceramics via high-energy ball-milling leads to ion conductors with, in many cases, greatly improved transport properties. By using both NMR and EXAFS we could show that for some of the samples prepared in planetary mills ($LiAlO_2$, $LiTaO_3$, $Li_2B_4O_7$) the formation of amorphous material plays indeed a decisive role in explaining the enhancement seen. For some of the oxides studied an upper limit of σ_{DC} is seen for sufficiently long periods of milling. Besides amorphous structures, the introduction of defects into the bulk regions of the nanocrystallites has also to be considered if samples prepared in shaker mills are to be studied. It turned out that, aside from few exceptions (see, e.g. $Li_4Ti_5O_{12}$, Li_2O_2), ion transport properties can be easily manipulated by tuning the degree of structural disorder. This strategy holds at least for oxides with low conductivities and, of course, depends on the exact crystal structure and bonding situations of the materials as well as their tendencies to form metastable modifications usually showing up at high temperatures or pressures. Fast ion conductors, on the other hand, may suffer rather than benefit from mechanically induced structural disorder.

Acknowledgements: We thank the Deutsche Forschungsgemeinschaft for financial support (FOR 1277, Mobility of Lithium Ions in Solids, sub-projects 7 and 1 (TP 7, TP 1), grant no. WI 3600 4-1(2) and 2-1(2)) over the last 6 years in the Research Unit 'molife'. Moreover, additional financial support by the Austrian Federal Ministry of Science, Research and Economy, and the Austrian National Foundation for Research, Technology and Development (in the frame of the Christian-Doppler-Laboratory of Lithium Batteries: Ageing Effects, Technology and New Materials) is greatly appreciated.

References

1. V. Šepelák, A. Düvel, M. Wilkening, K. D. Becker, P. Heitjans, Chem. Soc. Rev. **42**, 7507 (2013).
2. P. Heitjans, S. Indris, J. Phys. Condens. Matter **15**, R1257 (2003).
3. F. Preishuber-Pflügl, M. Wilkening, Dalton. Trans. **45**, 8675 (2016).

4. P. Heitjans, M. Masoud, A. Feldhoff, M. Wilkening, Faraday Discuss. **134**, 67 (2007).
5. M. Wilkening, V. Epp, A. Feldhoff, P. Heitjans, J. Phys. Chem. C **112**, 9291 (2008).
6. M. Wilkening, A. Düvel, F. Preishuber-Pflügl, K. da Silva, S. Breuer, V. Šepelák, P. Heitjans, Z. Krist.-Cryst. Mater. **32**, 107 (2016).
7. B. Ruprecht, M. Wilkening, S. Steuernagel, P. Heitjans, J. Mater. Chem. **18**, 5412 (2008).
8. B. Ruprecht, M. Wilkening, A. Feldhoff, S. Steuernagel, P. Heitjans, Phys. Chem. Chem. Phys. **11**, 3071 (2009).
9. A. Düvel, B. Ruprecht, P. Heitjans, M. Wilkening, J. Phys. Chem. C **115**, 23784 (2011).
10. A. V. Chadwick, Nature **408**, 925 (2000).
11. A. Chadwick, S. Savin, Solid State Ion. **177**, 3001 (2006).
12. J. Maier, Prog. Solid State Chem. **23**, 171 (1995).
13. J. Maier, Phys. Chem. Chem. Phys. **11**, 3011 (2009).
14. J. Maier, Nat. Mater. **4**, 805 (2005).
15. J. Maier, J. Phys. Chem. Solids **46**, 309 (1985).
16. J. Maier, Chem. Mater. **26**, 348 (2014).
17. J. Maier, Z. Phys. Chem. **217**, 415 (2003).
18. J. Schoonman, Solid State Ion. **157**, 319 (2003).
19. P. Knauth and J. Schoonman (Eds.), Nanocrystalline Metals and Oxides, Kluwer, Boston, MA (2001).
20. P. Heitjans, E. Tobschall, M. Wilkening, Eur. Phys. J. Spec. Top. **161**, 97 (2008).
21. P. Heitjans M. Wilkening, Mater. Res. Bull. **34**, 915 (2009).
22. P. Heitjans, M. Wilkening, Defect Diffus. Forum **283–286**, 705 (2009).
23. P. Knauth, J. Schoonman (Eds.), Nanocomposites – Ionic Conducting Materials and Structural Spectroscopies, Springer, New York (2008).
24. J. M. Laugier, L. Raymond, G. Albinet, P. Knauth, Modell. Simul. Mater. Sci. Eng. **19**, 065001 (2011).
25. P. Knauth, J. M. Debierre, G. Albinet, Solid State Ion. **121**, 101 (1999).
26. P. Knauth, G. Albinet, J. M. Debierre, Ber. Bunsenges. Phys. Chem. **102**, 945 (1998).
27. H. Brandstätter, D. Wohlmuth, P. Bottke, V. Pregartner, M. Wilkening, Z. Phys. Chem. **229**, 1363 (2015).
28. D. Wohlmuth, V. Epp, B. Stanje, A. M. Welsch, H. Behrens, and M. Wilkening, J. Am. Ceram. Soc. **99**, 1687 (2016).
29. A. Dunst, V. Epp, I. Hanzu, S. A. Freunberger, M. Wilkening, Energy. Environ. Sci. **7**, 2739 (2014).
30. V. Epp, M. Wilkening, ChemPhysChem **14**, 3706 (2013).
31. S. Indris, D. Bork, P. Heitjans, J. Mater. Synth. Process. **8**, 245 (2000).
32. S. Indris, P. Heitjans, Mater. Sci. Forum **343–343**, 417 (2000).
33. M. Wilkening, S. Indris, P. Heitjans, Phys. Chem. Chem. Phys. **5**, 2225 (2003).
34. A. S. Arico, P. Bruce, B. Scrosati, J. M. Tarascon, W. Van Schalkwijk, Nat. Mater. **4**, 366 (2005).
35. P. G. Bruce, B. Scrosati, J. M. Tarascon, Angew. Chem. Int. Ed. **47**, 2930 (2008).
36. Z. Liu, Y. G. Andreev, A. R. Armstrong, S. Brutti, Y. Ren, P. G. Bruce, Prog. Nat. Sci.-Mater. **23**, 235 (2013).
37. Y. Ren, Z. Liu, F. Pourpoint, A. R. Armstrong, C. P. Grey, P. G. Bruce, Angew. Chem. Int. Ed. **51**, 2164 (2012).
38. Y. Ren, A. R. Armstrong, F. Jiao, and P. G. Bruce, J. Am. Chem. Soc. **132**, 996 (2010).
39. Y. Ren, L. J. Hardwick, P. G. Bruce, Angew. Chem. Int. Ed. **49**, 2570 (2010).
40. T. Djenizian, I. Hanzu, P. Knauth, J. Mater. Chem. **21**, 9925 (2011).

41. G. F. Ortiz, I. Hanzu, P. Knauth, P. Lavela, J. L. Tirado, T. Djenizian, Electrochim. Acta **54**, 4262 (2009).
42. D. Prutsch, M. Wilkening, I. Hanzu, ACS Appl. Mater. Interfaces **7**, 25757 (2015).
43. P. Bottke, Y. Ren, I. Hanzu, P. G. Bruce, M. Wilkening, Phys. Chem. Chem. Phys. **16**, 1894 (2014).
44. M. Wilkening, J. Heine, C. Lyness, A. R. Armstrong, P. G. Bruce, Phys. Rev. B **80**, 064302 (2009).
45. M. Wilkening, C. Lyness, A. R. Armstrong, P. G. Bruce, J. Phys. Chem. C **113**, 4741 (2009).
46. A. Dunst, M. Sternad, M. Wilkening, Mat. Sci. Engin. B **211**, 85 (2016).
47. D. Wohlmuth, V. Epp, P. Bottke, I. Hanzu, B. Bitschnau, I. Letofsky-Papst, M. Kriechbaum, H. Amenitsch, F. Hofer, M. Wilkening, J. Mater. Chem. A **2**, 20295 (2014).
48. A. V. Chadwick, D. M. Pickup, S. Ramos, G. Cibin, N. Tapia-Ruiz, S. Breuer, D. Wohlmuth, M. Wilkening, Inst. Phys. Conf. Series Mat. Sci. Engin. **169**, 012015 (2017).
49. J. Langer, V. Epp, M. Sternad, M. Wilkening, Solid State Ion. **276**, 56 (2015).
50. M. J. Marczewski, B. Stanje, I. Hanzu, M. Wilkening, P. Johansson, Phys. Chem. Chem. Phys. **16**, 12341 (2014).
51. M. Wagemaker, A. P. M. Kentgens, F. M. Mulder, Nature **418**, 397 (2002).
52. M. Wagemaker, R. van de Krol, A. P. M. Kentgens, A. A. van Well, F. M. Mulder, J. Am. Chem. Soc. **123**, 11454 (2001).
53. V. Zwilling, E. Darque-Ceretti, A. Boutry-Forveille, D. David, M. Y. Perrin, M. Aucouturier, Surf. Interface Anal. **27**, 629 (1999).
54. D. Gong, C. A. Grimes, O. K. Varghese, W. Hu, R. S. Singh, Z. Chen, E. C. Dickey, J. Mater. Res. **16**, 3331 (2001).
55. R. Beranek, H. Hildebrand, P. Schmuki, Electrochem. Solid-State Lett. **6**, B12 (2003).
56. J. J. Kelly, Electrochim. Acta **24**, 1273 (1979).
57. M. Paulose, H. E. Prakasam, O. K. Varghese, L. Peng, K. C. Popat, G. K. Mor, T. A. Desai, C. A. Grimes, J. Phys. Chem. C **111**, 14992 (2007).
58. D. Regonini, C. R. Bowen, A. Jaroenworaluck, R. Stevens, Mat. Sci. Engin. R-Rep. **74**, 377 (2013).
59. D. Kowalski, D. Kim, P. Schmuki, Nano Today **8**, 235 (2013).
60. I. Hanzu, T. Djenizian, P. Knauth, ECS Transact. **35**, 21 (2011).
61. R. Böhmer, K. R. Jeffrey, M. Vogel, Prog. Nucl. Magn. Reson. Spectrosc. **50**, 87 (2007).
62. M. Wilkening, W. Küchler, P. Heitjans, Phys. Rev. Lett. **97**, 065901 (2006).
63. M. Wilkening, P. Heitjans, ChemPhysChem **13**, 53 (2012).
64. M. Wilkening, D. Gebauer, P. Heitjans, J. Phys. Condens. Matter **20**, 022201 (2008).
65. M. Wilkening, P. Heitjans, Phys. Rev. B **77** (2008).
66. M. Wilkening, P. Heitjans, Defect Diffus. Forum **237–240**, 1182 (2005).
67. M. Wilkening, P. Heitjans, J. Phys. Condens. Matter **18**, 9849 (2006).
68. M. Wilkening, A. Kuhn, P. Heitjans, Phys. Rev. B **78**, 054303 (2008).
69. R. Böhmer, T. Jörg, F. Qi, A. Titze, Chem. Phys. Lett. **316**, 419 (2000).
70. F. Qi, G. Diezemann, H. Böhm, J. Lambert, R. Böhmer, J. Magn. Reson. **169**, 225 (2004).
71. F. Qi, T. Jörg, R. Böhmer, Solid State Nucl. Magn. Reson. **22**, 484 (2002).
72. R. Böhmer, F. Qi, Solid State Nucl. Magn. Reson. **31**, 28 (2007).
73. P. Bottke, D. Rettenwander, W. Schmidt, G. Amthauer, M. Wilkening, Chem. Mater. **27**, 6571 (2015).
74. P. Heitjans, A. Schirmer, S. Indris, NMR and β-NMR studies of diffusion in interface-dominated and disordered solids. In: Diffusion in Condensed Matter – Methods, Materials, Models, (Eds. P. Heitjans, J. Kärger) Springer, Berlin (2005), P. 367.

75. V. Epp, M. Wilkening. Handbook of Solid State Batteries, World Scientific, Singapore (2015).
76. J. Heine, M. Wilkening, P. Heitjans, Diff. Fundam. **12**, 95 (2010).
77. A. Kuhn, S. Narayanan, L. Spencer, G. Goward, V. Thangadurai, M. Wilkening, Phys. Rev. B **83**, 094302 (2011).
78. H. Lindstrom, S. Sodergren, A. Solbrand, H. Rensmo, J. Hjelm, A. Hagfeldt, S. E. Lindquist, J. Phys. Chem. B **101**, 7717 (1997).
79. V. Epp, M. Wilkening, Phys. Rev. B **82**, 020301 (2010).
80. S. Nakhal, D. Wiedemann, B. Stanje, O. Dolotko, M. Wilkening, M. Lerch, J. Solid State Chem. **238**, 60 (2016).
81. B. Stanje, V. Epp, S. Nakhal, M. Lerch, M. Wilkening, ACS Appl. Mater. Interface **7**, 4089 (2015).
82. A. F. McDowell, C. F. Mendelsohn, M. S. Conradi, R. C. Bowman, A. J. Maeland, Phys. Rev. B **51**, 6336 (1995).
83. W. Küchler, P. Heitjans, A. Payer, R. Schöllhorn, Solid State Ion. **70**, 434 (1994).
84. M. Uitz, V. Epp, P. Bottke, M. Wilkening, J. Electroceram. in press (2016). DOI: 10.1007/s10832-017-0071-4.
85. V. Epp, S. Nakhal, M. Lerch, M. Wilkening, J. Phys. Condens. Matter **25**, 195402 (2013).
86. D. Wiedemann, S. Nakhal, J. Rahn, E. Witt, M. M. Islam, S. Zander, P. Heitjans, H. Schmidt, T. Bredow, M. Wilkening, M. Lerch, Chem. Mater. **28**, 915 (2016).
87. E. Witt, S. Nakhal, C. V. Chandran, M. Lerch, P. Heitjans, Z. Phys. Chem. **229**, 1327 (2015).
88. D. Wiedemann, S. Indris, M. Meven, B. Pedersen, H. Boysen, R. Uecker, P. Heitjans, M. Lerch, Z. Krist.-Cryst. Mater. **231**, 189 (2016).
89. J. Langer, D. Wohlmuth, A. Kovalcik, V. Epp, F. Stelzer, M. Wilkening, Ann. Phys. **527**, 523 (2015).
90. B. Ruprecht, M. Wilkening, R. Uecker, P. Heitjans, Phys. Chem. Chem. Phys. **14**, 11974 (2012).
91. K. Okada, N. Machida, M. Naito, T. Shigematsu, S. Ito, S. Fujiki, M. Nakano, Y. Aihara, Solid State Ion. **255**, 120 (2014).
92. Y. T. Li, J. T. Han, C. A. Wang, H. Xie, J. B. Goodenough, J. Mater. Chem. **22**, 15357 (2012).
93. L. Cheng, J. S. Park, H. M. Hou, V. Zorba, G. Y. Chen, T. Richardson, J. Cabana, R. Russo, M. Doeff, J. Mater. Chem. A **2**, 172 (2014).
94. M. Wilkening, R. Amade, W. Iwaniak, P. Heitjans, Phys. Chem. Chem. Phys. **9**, 1239 (2007).
95. W. Schmidt, M. Wilkening, Solid State Ion. **287**, 77 (2016).
96. W. Schmidt, P. Bottke, M. Sternad, P. Gollob, V. Hennige, M. Wilkening, Chem. Mater. **27**, 1740 (2015).
97. M. Wilkening, W. Iwaniak, J. Heine, V. Epp, A. Kleinert, M. Behrens, G. Nuspl, W. Bensch, P. Heitjans, Phys. Chem. Chem. Phys. **9**, 6199 (2007).
98. O. Gerbig, R. Merkle, J. Maier, Adv. Mater. **25**, 3129 (2013).
99. M. D. Radin, D. J. Siegel, Energy. Environ. Sci. **6**, 2370 (2013).
100. T. R. Krawietz, D. K. Murray, J. F. Haw, J. Phys. Chem. A **102**, 8779 (1998).
101. M. Lausch, H. W. Spiess, J. Magn. Reson. **54**, 466 (1983).
102. M. Lausch, H. W. Spiess, Chem. Phys. Lett. **71**, 182 (1980).
103. X. P. Tang, R. Busch, W. L. Johnson, Y. Wu, Bulk Metallic Glasses, Mater. Res. Soc. Symp. P **554**, 87 (1999).
104. X. P. Tang, R. Busch, W. L. Johnson, Y. Wu, Phys. Rev. Lett. **81**, 5358 (1998).
105. A. Kuhn, M. Wilkening, P. Heitjans, Solid State Ion. **180**, 302 (2009).
106. A. Kuhn, E. Tobschall, P. Heitjans, Z. Phys. Chem. **223**, 1359 (2009).
107. C. V. Chandran, P. Heitjans, Ann. Rep. NMR Spectrosc. **89**, 1 (2016).
108. P. Bottke, Diploma Thesis, Leibniz University Hannover (2010).